A Transient-Modeling-Based Grey-Box Method for Online Monitoring of DC-Link Capacitors

Zhao, Zhaoyang; Hu, Haitao; He, Zhengyou; Lu, Weiguo; Ho-Ching Iu, Herbert ; Blaabjerg, Frede; Davari, Pooya

Published in:
I E E E Transactions on Power Electronics

DOI (link to publication from Publisher):
10.1109/TPEL.2023.3308115

Publication date:
2023

Document Version
Accepted author manuscript, peer reviewed version

A Transient Modeling-Based Grey-Box Method for Online Monitoring of DC-Link Capacitors

Zhaoyang Zhao, *Member, IEEE*, Haitao Hu, *Senior Member, IEEE*, Zhengyou He, *Senior Member, IEEE*, Weiguo Lu, *Member, IEEE*, Herbert Ho-Ching Iu, *Senior Member, IEEE*, Frede Blaabjerg, *Fellow, IEEE*, and Pooya Davari, *Senior Member, IEEE*

***Abstract*—This paper proposes a suitable grey-box method for online monitoring of dc-link capacitors. It is found that the transient behavior of dc-link voltage in ac/dc and dc/dc converters is similar to the zero-state response of a parallel RLC circuit. Moreover, the damping factor α (related to capacitance) of the large-signal transient trajectories of converters can be chosen as a new health indicator of capacitors. Based on this, a nonintrusive transient equivalent circuit model (TECM)-based grey-box method is presented, which can realize the condition monitoring (CM) of dc-link capacitors with minimum dependency on the detailed topology and control information. Besides, it has features of relatively high applicability and extreme low sampling frequency requirement. Taking an ac/dc system and a dc/dc system as case studies, simulation results demonstrate the proposed method is suitable for converters with different load types. Moreover, a commercial power supply is chosen as an experimental case. Experimental results illustrate that the estimation errors of the damping factor α and dc-link capacitance are less than 1%. Furthermore, two typical application cases for a white-box system and a grey-box system are given to further illustrate the implementation of the proposed method.**

***Index Terms*—Condition monitoring, dc-link capacitor, grey-box method, transient modeling.**

I. Introduction

AC/DC and DC/DC converters are widely used in the front end of power conversion systems, such as communication base stations, motor drives, central processing units, etc [1]. In such applications, the loading of converter systems is frequently changed [2]. Usually, a large bulk capacitor bank is used in dc links (e.g., C_{dc} and C_o) to suppress ripple, absorb harmonics, balance instantaneous power, and store sufficient energy during transients [3]. However, the capacitor is one of the weakest links in power electronic converters [4], [5]. For reliability reasons, it is essential to realize condition monitoring (CM) of dc-link capacitors [6], [7].

Equivalent series resistance (ESR), capacitance (C), impedance (Z), etc., are widely used as health indicators of capacitors. Recently, many efforts have been made to realize the online estimation of health indicators of capacitors [8]–[39]. From the perspective of required information, they can be divided into three types, i.e., white-box method [8]–[26], grey-box method [27]–[34], and black-box method [35]–[39]. Table I summarizes the features and subcategories of these three types of methods. The typical implementation schemes for CM of dc-link capacitors are further summarized in Table II.

As shown in Table II, the system operation model-based schemes [8]–[17] (i.e., category A1), injected signal based-schemes [18]–[21] (i.e., category A2), and circuit

TABLE I
CLASSIFICATION OF TYPICAL CONDITION MONITORING METHODS FOR DC-LINK CAPACITORS

White box	Features	•On the basis of topology structure, operation mode and/or control strategy of converters
	Sub-categories	•**A1:** System operation model-based scheme [8]–[17] (e.g., build the relationship between capacitor parameters and steady-state ripples to estimate ESR/C) •**A2:** Injected signal-based scheme [18]–[21] (e.g., inject low-frequency signal to systems, and estimate C at the corresponding frequency) •**A3:** Circuit parameters model-based scheme [22]–[26] (e.g., identify the parameters of built circuit model)
Grey box	Features	•Without any knowledge of operation mode and/or control strategy of converters •Requiring knowledge of connection structure •Estimation model is available for other types of converters
	Sub-categories	•**B1:** Capacitor current directly measurement scheme [27]–[33] (e.g., sample capacitor voltage and current to estimate parameters) •**B2:** Switching ringing-based scheme [34] (e.g., analyze the switching ringing of dc-link current to estimate ESR)
Black box	Features	•Without any knowledge of circuit structure, operation mode and/or control strategy of converters •Need a large amount of training data and labels •Estimation model needs retraining when used for other converters
	Sub-categories	•**C1:** Data-driven scheme [36]–[39] (e.g., use intelligent algorithms to train voltage and current data to obtain C)

Manuscript received 7 April 2023; revised 12 July 2023; accepted 20 August 2023. This work was supported in part by the National Natural Science Foundation of China under Grant 52207225, in part by the Sichuan Science and Technology Program under Grant 2022NSFSC0001, in part by the Natural Science Foundation of Sichuan Province under Grant 2023NSFSC0814, and in part by the Central University Science and Technology Innovation Project under Grants 2682022ZTPY070, 2682022KJ029, and 2682023CX004. (*Corresponding author: Haitao Hu.*)

Zhaoyang Zhao, Haitao Hu, and Zhengyou He are with the National Rail Transportation Electrification and Automation Engineering Technology Research Center, Southwest Jiaotong University, Chengdu 610031, China (e-mail: zhaoyang.zhao@swjtu.edu.cn; hht@swjtu.edu.cn; hezy@swjtu.edu.cn).

Weiguo Lu is with the State Key Laboratory of Power Transmission Equipment & System Security and New Technology, Chongqing University, Chongqing 400044, China (e-mail: luweiguo@cqu.edu.cn).

H. H.-C. Iu is with the School of Electrical, Electronics and Computer Engineering, University of Western Australia, Crawley, WA 6009, Australia (e-mail: herbert.iu@uwa.edu.au).

Frede Blaabjerg and Pooya Davari are with the AAU Energy, Aalborg University, 9220 Aalborg, Denmark (email: fbl@energy.aau.dk; pda@energy.aau.dk).

TABLE II
TYPICAL IMPLEMENTATION SCHEMES FOR CM OF DC-LINK CAPACITORS

Type	Ref	Topology (control)	f_{sw} (N)	Used signal	Additional sampling circuits/devices	Estimation error	Advantages and limitations
A1	[8]	Buck (N/A)	100 kHz (N/A)	v_o, i_L	Rogowski coil sensor, oscilloscope (HF sampling and calculation)	ESR: <5.6%	☑ Switch fault diagnosis and ESR estimation ☒ Specially designed current sensor, high-frequency sampling, specific topology
	[9]	Boost (analog)	30 kHz (N=333)	v_o, i_L	Ripples extraction circuit, data acquisition card	ESR: <3.1%	☑ No additional current sensor ☒ Additional hardware circuits, high-frequency sampling, specific topology
	[10]	Boost PFC (analog)	60 kHz (N=53.3)	v_o, i_L	Ripples extraction circuits, trigger circuits, MCU	ESR: <10%	
	[11]	PV boost (digital)	10 kHz (N=4)	v_{pv}, i_{pv}	Ripples extraction circuit, MCU (controller)	ESR: <6.2%	☑ Relatively low sampling frequency, no additional current sensor ☒ Additional hardware circuits, specific topology
	[12]	Flyback (analog)	100 kHz (N=2)	v_o, v_i, v_{pwm}	Ripples extraction circuit, pulse capture circuit, MCU	ESR: <3.1% C: <3.7%	
	[13]	Boost PFC (analog)	66 kHz (N=2)	v_o, v_i, i_L	Ripples extraction circuits, PWM trigger circuits, MCU	ESR: <3.7% C: <1.9%	
	[14]	LLC (analog)	82.6 kHz (N/A)	v_o, i_o	Ripples extraction circuits, load current sensor, MCU	ESR: <1.5%	☑ Ripple valley and peak search ☒ Specific topology, additional current sensor and hardware
	[15]	ASD (N/A)	N/A	v_r, v_{dc}	Not given	ESR: <5.48% C: <1.1%	☑ No additional current sensor and hardware circuits ☒ Quasi-online, specific topology and operation condition
	[16]	PV inverter (digital)	10 kHz (N=1)	v_{pv}, i_{pv}, d	N/A	C: <2.6%	☑ No additional current sensor and hardware circuits ☒ Specific topology
	[17]	ASD (digital)	10 kHz (N/A)	v_{dc}, i_g, i_d, i_q	N/A	C: <1%	
A2	[18]	PV inverter (digital)	10 kHz (N/A)	v_{dc}, v_g i_L, d	Ripples extraction circuits	ESR<3.65% C: <1.88%	☑ No additional current sensor ☒ Quasi-online, additional hardware, specific topology
	[19]	Inverter (digital)	4 kHz (N/A)	v_{dc}, i_{sc}	Oscilloscope (HF sampling)	ESR<6%	☑ No additional current sensor and hardware circuits ☒ High-frequency sampling during the test
	[20]	ASD (digital)	5 kHz (N=2)	v_{dc}, i_a, i_b, i_c, d	N/A	C: <1%	☑ No additional current sensor and hardware circuits ☒ Specific topology and operation condition
	[21]	ASD (digital)	10 kHz (N=2)		N/A	C: <1%	
A3	[22]	PV buck (digital)	1 kHz (N=10)	v_o, i_L, v_i, v_{pwm}	Data acquisition card	C: <5%	☑ Full parameters monitoring ☒ Specific topology, high-frequency sampling
	[23]	Boost (N/A)	30 kHz (N=333)	v_o, i_L	Oscilloscope (HF sampling)	ESR<11.7% C: <9.2%	
	[24]	PV boost (digital)	10 kHz (N=1)	v_{pv}, i_{pv}, i_L	Ripples extraction circuits	Z: <0.7%	☑ Relatively low sampling frequency ☒ Specific topology, additional hardware circuits, no detail values of ESR or C
	[25]	Buck (digital)	20 kHz (N=1)	v_o, i_L, d	N/A	ESR<10.9% C: <18.6%	☑ No additional current sensor and hardware circuits ☒ Specific topology, relatively complex algorithm
	[26]	Buck (digital)	20 kHz (N=2.5)	v_o, i_L	N/A	C: <6.1%	
B1	[27]	PV boost (digital)	20 kHz (N=50)	v_c, i_c	Capacitor current sensor, oscilloscope (HF sampling)	ESR<5.6%	☑ Relatively high applicability ☒ Additional current sensors [27]–[32], high-frequency sampling [27]–[31]
	[28]	Boost (N/A)	5 kHz (N=20)	v_c, i_c	Capacitor current sensor, data acquisition card	ESR<6.34% C: <2.63%	
	[29]	Boost (N/A)	20 kHz (N=26)	v_c, i_c	Capacitor current probe, oscilloscope (HF sampling)	ESR<3%	
	[30]	Inverter (N/A)	3 kHz (N=26)	v_c, i_c	Capacitor current sensor, ripple sampling devices	Not given	
	[31]	ASD (digital)	2.5 kHz (N is about 4)	v_c, i_c	Capacitor current sensor, ripples extraction circuits	ESR<3% C: <1%	
	[32]	ASD (N/A)	2 kHz (N/A)	v_c, i_c	Capacitor current sensor, MCU	ESR<1.8%	
	[33]	Inverter (N/A)	12.5 kHz (N=8)	v_c, i_c	Rogowski coil sensor, ripples extraction circuits	ESR<1.9%	☑ Single capacitor monitoring, high applicability ☒ Additional sensors and hardware
B2	[34]	ASD (N/A)	5 kHz (N=2^{15})	i_{dc}	Capacitor current sensor, oscilloscope (HF sampling)	ESR<1.8%	☑ High applicability ☒ Additional current sensor
C1	[36]	ASD (N/A)	N/A	v_{dc}, v_i, C_{la}	Oscilloscope (HF sampling)	C: <1.3%	☑ High accuracy ☒ High-frequency sampling, a large amount of training data and labels, complex algorithms, retraining for other topologies
	[37]	Inverter-EMI filter (N/A)	20 kHz (N=50)	EMI, C_{la}, ESR_{la}	Oscilloscope (HF sampling)	N/A	
	[38]	Inverter (N/A)	5 kHz (N=50)	i_s, C_{la}, ESR_{la}	Oscilloscope (HF sampling)	ESR<0.1% C: <0.1%	
	[39]	Inverter (N/A)	5 kHz (N=50)	v_c, i_c, C_{la}, ESR_{la}	Oscilloscope (HF sampling)	ESR<0.11% C: <0.11%	
Transient idea	[40]	Buck (analog and digital)	200 kHz (N=1)	v_o, i_o	Load current sensor, transient detection circuits	ESR<7.4% C: <9.6%	☑ Relatively low sampling frequency ☒ Specific topology [40]–[42], additional sensors and circuits [40], [41]
	[41]	Boost (digital)	200 kHz (N=1)	v_o, i_o, d	Load current sensor	C: <3%	
	[42]	Boost PFC (digital)	50 kHz (N=1)	v_i, i_s, v_o, d	N/A	C: <3.5%	
Proposed method		Front-end ac/dc	100 kHz (N=1/4, 1/40)	v_{dc}	• Voltage sensor (for grey-box systems) • N/A (for white-box systems)	α: <1%	☑ Extremely low sampling frequency, suitable for grey-box systems with minimum dependency on the detailed topology and control information, high applicability, no additional sensors for white-box systems ☒ A pre-test is needed if the capacitance is estimated
		Rear-end dc/dc	125 kHz (N=1, 1/2)	v_o			

Note: Power factor correction (PFC), photovoltaic (PV), adjustable speed drive (ASD), electromagnetic interference (EMI), microcontroller unit (MCU), high-frequency (HF), switching frequency (f_{sw}), the number of sampling points during one switching cycle (N), output voltage (v_o), inductor current (i_L), input voltage (v_i), output current (i_o), rectified voltage of ASD with a diode rectifier (v_r), dc-link voltage (v_{dc}), PWM signal (v_{pwm}), PV voltage (v_{pv}), PV current (i_{pv}), control signal and/or duty cycle (d), rectified grid current of VSD (i_g), motor current of the dq-axis (i_d, i_q), grid voltage (v_g), short-circuit current (i_{sc}), motor current (i_a, i_b, i_c), capacitor voltage (v_c), capacitor current (i_c), dc-bus current (i_{dc}), training labels (C_{la}, ESR_{la}), source current (i_s), advantages (☑), limitations (☒).

parameters model-based-schemes [22]–[26] (i.e., category A3) can be considered as white-box methods. Generally, the topology structure, operation modes, ripple information, and/or control signals of converters are required in white-box methods. Therefore, some additional current sensors [8], [14], ripple extraction circuits [9]–[14], [18], [24] and/or high-speed sampling devices [8]–[10], [19], [22], [23], etc., are required to obtain the key information of converters. Although the schemes in [15]–[17], [20], [21], [25], and [26] do not require additional current sensor and hardware circuits, specific topologies,

digital controllers, and/or specific operation conditions are required, which reduces their extensibility.

Different from that of white-box methods, only partial knowledge of converters is required in grey-box methods. Referring to Table II, the capacitor current directly measurement schemes (i.e., category B1) [27]–[33] and switching ringing-based schemes (i.e., category B2) [34] can be considered as grey-box schemes. Generally, the grey-box schemes can be applied in all types of dc-link applications. However, the voltage/current ripples and switching ringing have the features of high frequency and small amplitude. Additional current sensors [27]–[34] and high-frequency sampling devices [27], [29], [34] are needed to obtain the sampling information accurately.

Moreover, data-driven-based black-box schemes (i.e., category C1) have been presented for CM of dc-link capacitors in [36]–[39]. Although they can realize the CM of capacitors without any knowledge of circuit structure, operation mode and/or control strategy of converters, complex training algorithms, a large amount of training data (e.g., output current and dc-link voltage ripples [36]), and labels (e.g., C [36]) are required. The complexity of software is larger than that of white-box and grey-box schemes. In addition, voltage and current ripples of converters are usually taken as training data, which results in the requirement of high-frequency sampling devices [36]–[39]. Besides, an estimation model for one converter topology needs retraining when used for other converter topologies [35], which limits their applicability to other converters.

In order to reduce the sampling frequency, the authors have presented a transient-based idea for CM of dc-link capacitors [40]–[42]. However, the estimation models in [40]–[42] are specially designed for one type of converter, which cannot be applied in other types of topologies. They are white-box schemes. Moreover, additional current sensors [40], [41] or specific digital controllers [42] are required, which limits their applicability to other topologies.

Considering that the grey-box scheme has good applicability, it is essential to develop a simple noninvasive CM scheme with minimum dependency on the detailed topology and control information. As a continuous research in [40]–[42] for exploring the transient-based CM schemes, it is found that the transient behavior of the dc-link voltage in ac/dc and dc/dc converters is similar to the zero state response of a parallel RLC circuit. Moreover, the damping factor α (related to capacitance) of transient trajectories of converters can be chosen as a new health indicator of capacitors. Based on this, this paper proposes a transient model-based grey-box scheme, which is a detailed expansion of the authors' granted patent [43]. It has the following advantages:

1) The proposed scheme is suitable for grey-box systems with minimum dependency on the detailed topology and control information.

2) Only transient voltage is required for CM, which does not need current information. Generally, an additional voltage sensor is required if the method is applied for a commercial converter without detailed topology and control information (i.e., a grey-box system). Fortunately, the voltage sensor for control purposes can be reused for CM if the monitoring function has been integrated into a converter in the design phase. The voltage sampled for the control purpose can be used for CM, and additional sensors are not required.

3) The sampling frequency of the utilized monitoring signal is extremely low, which can reduce the hardware cost of sampling systems and the volume of sampled data.

4) It has high applicability and can be used for ac/dc and dc/dc converters.

The rest of this paper is organized as follows. Section II describes the proposed TECM-based grey-box method. The simulation studies and experimental verification are drawn in Section III and Section IV, respectively. Furthermore, two typical application cases for a white-box system and a grey-box system are given in Section V. Finally, the conclusions are given in Section VI.

II. Proposed TECM-Based Grey-Box Method

As discussed in [40]–[42], the transient trajectory of power converters has the features of large amplitude and long duration (usually in the order of 1 ms [42]), which is easier to be sampled when compared with small-amplitude steady-state ripples. In order to reduce the sampling complexity and improve the applicability of CM schemes for commercial converters with minimum dependency on the detailed topology and control information, a nonintrusive transient equivalent circuit model (TECM)-based grey-box CM method is introduced in this section.

A. Transient Behavior Analysis

Generally, the transient response of an ac/dc or dc/dc converter is approximated by the dominant pole pair in the closed-loop pole-zero map. The load transient behavior of converters is similar to a zero-state response of a parallel RLC circuit [44]. Based on this, an ac/dc or dc/dc converter can be equivalent to an RLC circuit during load transients. Fig. 1(a) shows a converter system and its transient equivalent circuit, where C_{dc} represents the dc-link capacitor, v_{dc} and V_{ref} denote the dc-link voltage and its reference value, i'_{dc} represents the average value of rear-end current i_{dc}. L_{eq}, R_{eq} represent the inductance and resistance of RLC equivalent circuits, respectively. Δv is the output voltage of the RLC circuit. v'_{dc} represents the equivalent circuit voltage, which can be calculated as $v'_{dc} = \Delta v + V_{ref}$.

Taking a PFC-LLC converter as an example, Fig. 1(b) shows the simulation waveforms for a 250-W loading transient, where the circuit structure and control parameters of converters are the same as that in [42]. The capacitance of C_{dc} is 470 μF. Referring to Fig. 1(a), assuming L_{eq} and R_{eq} are 2.8 H and 90 Ω, Fig. 1(b) shows the output voltage v'_{dc} of the equivalent circuit. It can be seen that v'_{dc} is coincide with v_{dc}, which demonstrates that the RLC equivalent circuit can denote the load transient behavior of converters. Notice that L_{eq} and R_{eq} are related to the dynamic performance of converters, they have no physical meaning. In this example, L_{eq} and R_{eq} (i.e., 2.8 H and 90 Ω) are obtained from the parameter identification of the proposed transient model. Although they are related to the circuit parameters, they

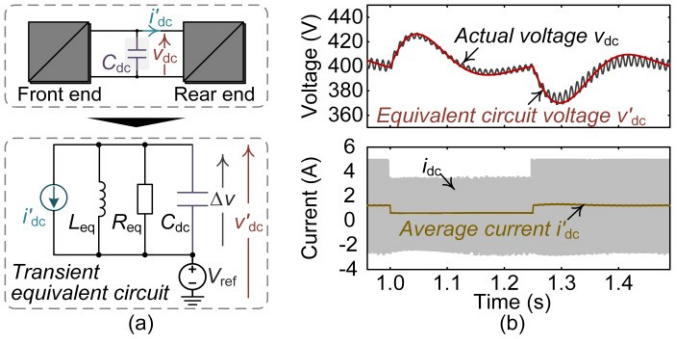

Fig. 1. Transient equivalent circuit and typical transient waveforms. (a) Transient equivalent circuit of ac/dc and dc/dc power converters. (b) Typical transient response waveforms of a PFC-LLC converter.

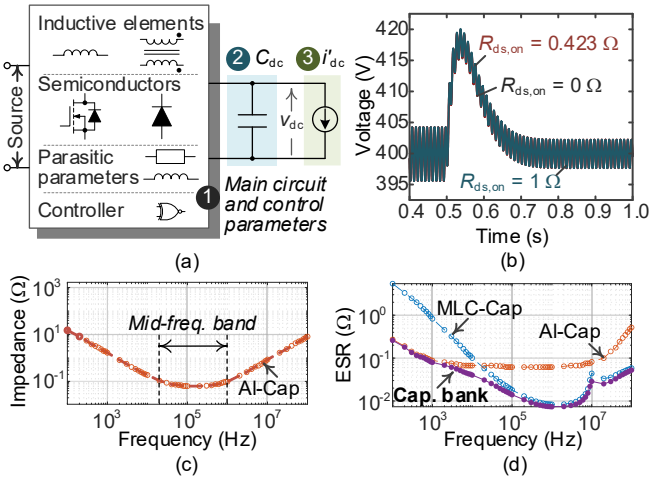

Note: the types of the aluminum electrolytic capacitor (Al-Cap) and the multi-layer ceramic capacitor (MLC-Cap) are WCAP-ATET-860130878011 [47] and GCJ31CR72A105KA01 [48], respectively. The capacitor bank is consisting of one Al-Cap and one MLC-Cap.

Fig. 2. Power converters' general structure, simulation waveforms of parameters drift, and the impedance characteristics of capacitors. (a) General structure of a power converter. (b) Simulation waveforms of parameters drifts. (c) Impedance of a capacitor [47]. (d) ESR of capacitors [47], [48].

cannot be obtained from the actual converter due to the control parameters also determines the transient trajectory. A detailed explanation is given in the following.

Fig. 2(a) shows the general structure of an ac/dc or dc/dc converter. Generally, a converter can be divided into three parts from the perspective of transient-related factors. One is the main circuit parameters (including inductive elements, power semiconductors, and parasitic parameters) and control parameters, which are equivalent to R_{eq} and L_{eq} of the transient equivalent circuit. The other two are the dc-link capacitance and transient step current, which are equivalent to C_{dc} and i'_{dc}. Usually, the control parameters of a converter are not changed once the design stages of converters have finished. However, the main circuit parameters may change with the degradation of components, especially power semiconductor switches [6], [45], [46]. Considering the parameter drift of MOSFETs, Fig. 2(b) gives the simulation waveforms of the above-mentioned PFC converter [42]. Here, three different on-resistances $R_{ds,on}$ of MOSFET are considered, i.e., $R_{ds,on}$ =0 Ω (indicating an ideal switch), $R_{ds,on}$ =0.423 Ω (indicating a fresh MOSFET [45]), and $R_{ds,on}$ =1 Ω (indicating an aged MOSFET [45]). The other circuit and control parameters of the converter are the same as that in [42]. It is found that the parameter drift almost has no effect on the transient trajectory. Notice that an inductive element is less prone to aging [6], which is not considered in the simulation. Based on the above analysis, it can be said that R_{eq} and L_{eq} are usually constant, and the transient trajectory is mainly dependent on capacitance and load current. It should be noted that the cases that indicate the effect of capacitance and load current on transient trajectories can be found in Section III.

On the other hand, the impedance of capacitors is dominated by ESR at a mid-frequency band and it is determined by C at a low-frequency band [c.f., Fig. 2(c)], which results in high-speed sampling is usually required to obtain the mid-frequent ripple information to estimate ESR [3]. Moreover, a small-capacity ceramic capacitor or a film capacitor is widely connected in parallel with electrolytic capacitors, which results in the total ESR of hybrid capacitor banks at the mid-frequency band cannot represent the actual ESR of electrolytic capacitors, as shown in Fig. 2(d). Furthermore, the repetitive frequency of load transients is relatively low (e.g., 1–10 Hz [42]). Therefore, a capacitor's impedance is dominated by C at the repetitive frequency (i.e., low-frequency bands). The ESR is not considered in the proposed equivalent circuit, and the capacitance (or capacitance-related parameter) is chosen as a health indicator. The proposed method is more suitable for the CM of hybrid capacitor banks, pure ceramic capacitor, and film capacitor banks.

B. Transient Behavior Modeling

As discussed above, the transient trajectory of v_{dc} (i.e., Δv), can be modeled by an RLC circuit. Taking the unloading transient as an example, Fig. 3(a) shows the detailed transient response waveforms. Assuming that an unloading transient occurs at the instant t_0 (the step amplitude of i'_{dc} is ΔI), the voltage response of a parallel RLC circuit is [44]

$$\Delta v(t) = B_1 e^{-\alpha t}\cos(\omega_d t) + B_2 e^{-\alpha t}\sin(\omega_d t). \quad (1)$$

B_1 is constant, which is determined by the initial energy storage in the RLC circuit. For the zero-state response, $B_1=\Delta v\,(0^+) = 0$.

Therefore, (1) is rewritten as

$$\Delta v(t) = B_2 e^{-\alpha t}\sin(\omega_d t). \quad (2)$$

where α is the damping factor, which determines how quickly the oscillations subside. It is dependent on the capacitance and resistance of the equivalent RLC circuit, i.e.,

$$\alpha = 1/(2R_{eq}C_{dc}). \quad (3)$$

ω_d denotes the damped radian frequency, i.e.,

$$\omega_d = \sqrt{\omega_0^2 - \alpha^2} \quad (4)$$

where ω_0 represents the resonant radian frequency. It is calculated as

$$\omega_0 = 1/(L_{eq}C_{dc}). \quad (5)$$

B_2 is also a constant, which is dependent on the initial value and di/dt of i'_{dc}. Referring to Fig. 3(a), for an ideal step response, B_2 is denoted as

$$B_2 = \Delta I/(\omega_d C_{dc}). \quad (6)$$

Referring to (2)–(6), C_{dc} can be estimated based on the tran-

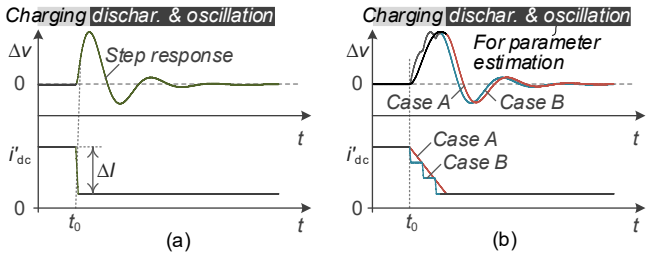

Fig. 3. Examples of transient waveforms. (a) Transient waveforms of a load step response. (b) Transient waveforms of gradual load change.

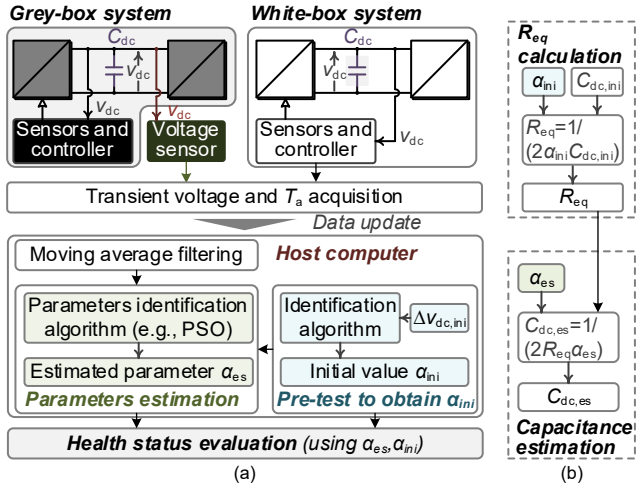

Note 1: The grey-box system mainly refers to commercial converters without detailed topology and control parameters.

Note 2: The white-box system mainly refers to converters in design and development stages. The voltage can be obtained using the existing sensors.

Fig. 4. Implementation flowchart of the proposed TECM-based scheme. (a) Flowchart for α estimation. (b) Flowchart for capacitance estimation.

sient voltage profile $\Delta v(t)$ and current step value ΔI. However, a current sensor is required if (6) is used. Referring to (3), it is found that C_{dc} is inversely correlated with α. As discussed in Part A, R_{eq} of a converter is usually constant. Therefore, α is chosen as a health indicator of capacitors in the proposed scheme.

Referring to Fig. 3(b), i'_{dc} may not suddenly change in some applications, e.g., Case A (relatively low di/dt) and Case B (multiple step). Considering the shape (e.g., time constant and oscillation period, not including oscillation amplitude) of transient voltage trajectory mainly depends on α and ω_d, which is not related to the initial current value and di/dt [44]. The transient voltage trajectory during discharging and oscillation stage can be chosen for parameter estimation for a non-ideal step response (i.e., the case that i'_{dc} is not suddenly changed).

In summary, the proposed TECM method utilizes the transient voltage trajectory to estimate the capacitance-related parameter α. The detailed implementation scheme is given in the following part.

C. Proposed TECM-Based CM Scheme

Fig. 4(a) shows the implementation flowchart of the proposed TECM-based scheme. Generally, the proposed scheme can realize the CM of capacitors in a grey-box system (e.g., commercial converters) and a white-box system (e.g., self-designed converters with the sampling of v_{dc}). However, an additional voltage sensor is required if the power converter can-

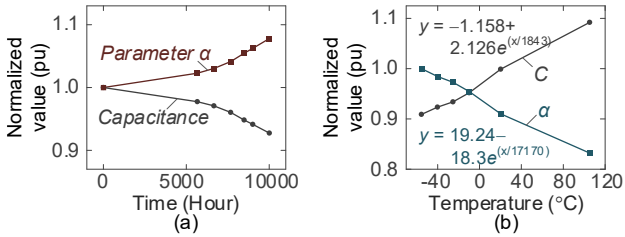

Fig. 5. Relationship between α and C [49]. (a) α and C versus aging time. (b) α and C versus aging temperature.

not provide the signal of v_{dc}.

In the proposed scheme, a parameter identification algorithm, such as the particle swarm optimization (PSO) algorithm [26], [35], is used to find the optimal solutions of (2), in order to fit the sampled transient voltage Δv_{dc} and obtain the capacitance-related parameter α, i.e.,

$$\underset{\alpha,B_2,\omega_d}{\operatorname{argmin}} f_{obj} = \sum_{j=1}^{n}\left(\Delta v_{dc,j} - \Delta v_{dc,m,j}\right)\Big/ N \tag{8}$$

where, $\Delta v_{dc,m,j}$ is the sampled transient voltage profile, $\Delta v_{dc,j}$ is the calculated transient voltage. N represents the number of data points.

Generally, capacitors' health status can be evaluated based on the comparison of online monitoring values and initial values. Here, a pre-test is required to sample the transient voltage $\Delta v_{dc,ini}$ to obtain the initial value α_{ini}, as shown in Fig. 4(a). Although the proposed scheme is mainly designed for the monitoring of α, capacitance $C_{dc,es}$ can be online estimated using (3). However, R_{eq} needs to be obtained in the pre-test, as shown in Fig. 4(b). Usually, an Al-Cap is considered failed when its capacitance has decreased by 20% of the initial value. Taking NIPPON Chemi-Con's Al-Cap as an example, Fig. 5(a) shows the degradation curve of capacitance [49]. Based on (3), the relationship between α and aging time can be derived, which is also demonstrated in Fig. 5(a). Usually, R_{eq} of a converter is constant. The failure criteria can be defined as $\alpha_{es}/\alpha_{ini} \geq 120\%$ if α is chosen as the health indicator, where α_{es} and α_{ini} represent the estimation value and initial value, respectively.

Assuming the initial capacitance is $C_{dc,ini}$, α_{ini} can be derived using the parameter identification algorithm and transient voltage profile $v_{dc,ini}$ in a pre-test. On the other hand, the capacitance is easily affected by ambient temperature T_a, a calibration of $C_{dc,ini}$ and α_{ini} should be considered, i.e.,

$$X_{ini}\left(T_a\right) = a + be^{-T_a/c} \tag{9}$$

where X_{ini} represents the values of $C_{dc,ini}$ and α_{ini}. a, b, and c are characteristic coefficients of capacitors. For NIPPON Chemi-Con's Al-Caps, Fig. 5(b) shows the normalized parameters versus temperature [49].

Notice that the transient voltage acquisition is implemented by comparing sampled voltage and the reference voltage, which can be implemented by a microcontroller unit (MCU). Also, a moving average filtering algorithm is used to filter the noise signals. The transient voltage acquisition and filter algorithms are detailed discussed in [42]. Moreover, the data processing is implemented in a host computer, which is similar to that in [10].

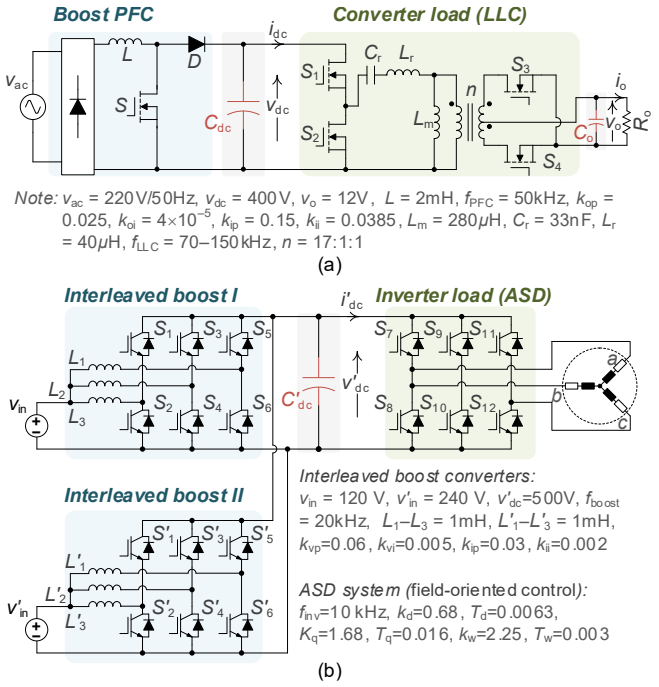

Fig. 6. Typical ac/dc and dc/dc systems with converter and inverter loads. (a) PFC-LLC converter. (b) Interleaved boost converters with an ASD load.

III. Simulation Verification

In order to verify the proposed CM method, typical ac/dc and dc/dc systems with converter and inverter loads are built in the PSIM simulation environment.

Fig. 6(a) shows the structure of an ac/dc system, where the front end and rear end are a boost PFC converter and an LLC converter, respectively. The detailed circuit parameters are given in the bottom of Fig. 6(a), where C_{dc} and C_o represent the dc-link capacitors and output capacitors, respectively. v_{ac}, v_{dc}, v_o, i_{dc} and i_o denote the input voltage, dc-link voltage, output voltage, dc-link current and output current, respectively. L, f_{PFC}, k_{op}, k_{oi}, k_{ip}, and k_{ii} are the switching frequency, inductance, voltage-loop proportion, voltage-loop integral, current-loop proportion, and current-loop integral coefficients of the PFC converter. L_m, C_r, L_r, f_{LLC} and n represent the transformer's magnetizing inductance, resonant capacitance, resonant inductance, switching frequency and transformer turns ratio of LLC converters.

Fig. 6(b) gives the structure of the built dc/dc system with an inverter load. The dc/dc system consists of two interleaved boost converters connected in parallel. The inverter load is an adjustable speed drive (ASD) system. The detailed circuit parameters are shown in the bottom of Fig. 6(b), where C'_{dc}, v_{in}, v'_{in}, v'_{dc} and i'_{dc} denote the dc-link capacitors, input voltages, dc-link voltage and dc-link current, respectively. L_1–L'_3, k_{vp}, k_{vi}, k_{ip}, and k_{ii} denote the inductances, voltage-loop proportion, voltage-loop integral, current-loop proportion, and current-loop integral coefficients boost converters, respectively. f_{inv}, k_d, T_d, k_q, T_q, k_w, and T_w represent the switching frequency, d-axis proportion, d-axis time constant, q-axis proportion, q-axis time constant, speed-loop proportion, speed-loop time constant, respectively.

TABLE III
DIFFERENT SIMULATION CONDITIONS FOR 17 CASES

	Cases	Simulation conditions
Boost PFC	I	***C*=470μF**, ESR=10mΩ, ΔP=250 W, LLC load
	II	***C*=430μF, ESR=50mΩ**, ΔP=250 W, LLC load
	III	***C*=510μF**, ESR=50mΩ, ΔP=250 W, LLC load
	IV	C=470μF, ESR=10mΩ, ΔP=250 W, LLC load, **v_{dc} decreases region**
	V	C=430μF, ESR=10mΩ, ΔP=250 W, LLC load, **v_{dc} decreases region**
	VI	C=510μF, ESR=10mΩ, ΔP=250 W, LLC load, **v_{dc} decreases region**
	VII	C=470μF, ESR=10mΩ, **ΔP=150 W**, LLC load
	VIII	C=470μF, ESR=10mΩ, **ΔP=350 W**, LLC load
	IX	C=470μF, ESR=10mΩ, ΔP=250 W, resistance load, **1-time step**
	X	C=470μF, ESR=10mΩ, ΔP=250 W, resistance load, **2-time step**
	XI	C=470μF, ESR=10mΩ, ΔP=250 W, resistance load, **3-time step**
LLC	XII	***C*=220μF**, ESR=5mΩ, ΔP=250 W
	XIII	***C*=190μF**, ESR=5mΩ, ΔP=250 W
	XIV	***C*=250μF**, ESR=5mΩ, ΔP=250 W
dc/dc with ASD	XV	***C*=470μF**, ESR=10mΩ, the speed changing value is 1800 r/min
	XVI	***C*=430μF**, ESR=10mΩ, the speed changing value is 1800 r/min
	XVII	***C*=510μF**, ESR=10mΩ, the speed changing value is 1800 r/min

Based on the built simulation models, 17 cases are chosen to verify the proposed method. Here, different simulation conditions are considered, including capacitor parameters (Cases I–III), transient regions (Cases IV–VI), transient amplitudes (Cases VII and VIII), change rates of transient current (Cases IX–XI), topology structures (Cases VII–XVII). The detailed simulation conditions are summarized in Table III.

A. Case Study of Boost PFC Converters

1) *Effect of Capacitor Parameters and Transient Regions*

Taking a 250-W unloading transient as a case study, Fig. 7(a) shows the simulation waveforms of Cases I–VI. It can be seen that the transient waveforms are mainly dependent on the capacitance. Generally, the maximum voltage deviation decreases as capacitance increases. However, ESR has a relatively small effect on transient voltage profiles.

Utilizing the PSO algorithm, Fig. 7(d) shows the fitted waveforms of transient voltage Δv_{dc}. It is found that the fitted waveforms are consistent with the simulation waveforms, which demonstrates the feasibility of the transient model (2). The corresponding fit parameters of α, B_2, and ω_d are shown in Table IV. In order to evaluate the estimation accuracy, a pre-test of Case I is taken to obtain R_{eq}. In the pre-test, the initial capacitance $C_{dc,ini}$ is 470 μF, and the fitted result of α_{ini} is 13.15. Then, R_{eq} of the boost PFC converter is calculated as 80.92. Based on this, estimated capacitances of Cases I–III are summarized in Table IV. It is found that the estimation errors are less than 1%, which demonstrates the feasibility of the proposed TECM-based method.

Referring to Fig. 7(a), the whole regions of transient profiles (i.e., the periods from 0.5 s to 0.8 s) are used to estimate capacitor parameters in Cases I–III. In Cases IV–VI, different transient regions are considered, i.e., the voltage-decrease regions (the periods from 0.54 s to 0.8 s). Fig. 7(e) shows the fitted waveforms of voltage-decrease regions. The results in Table IV demonstrate that the proposed scheme is feasible when different transient regions are used for parameter fitting.

2) *Effect of Transient Amplitudes*

Considering different transient amplitudes, Fig. 7(b) shows the simulation waveforms of 150-W and 350-W unloading transients (i.e., Cases VII and VIII). It can be seen that the

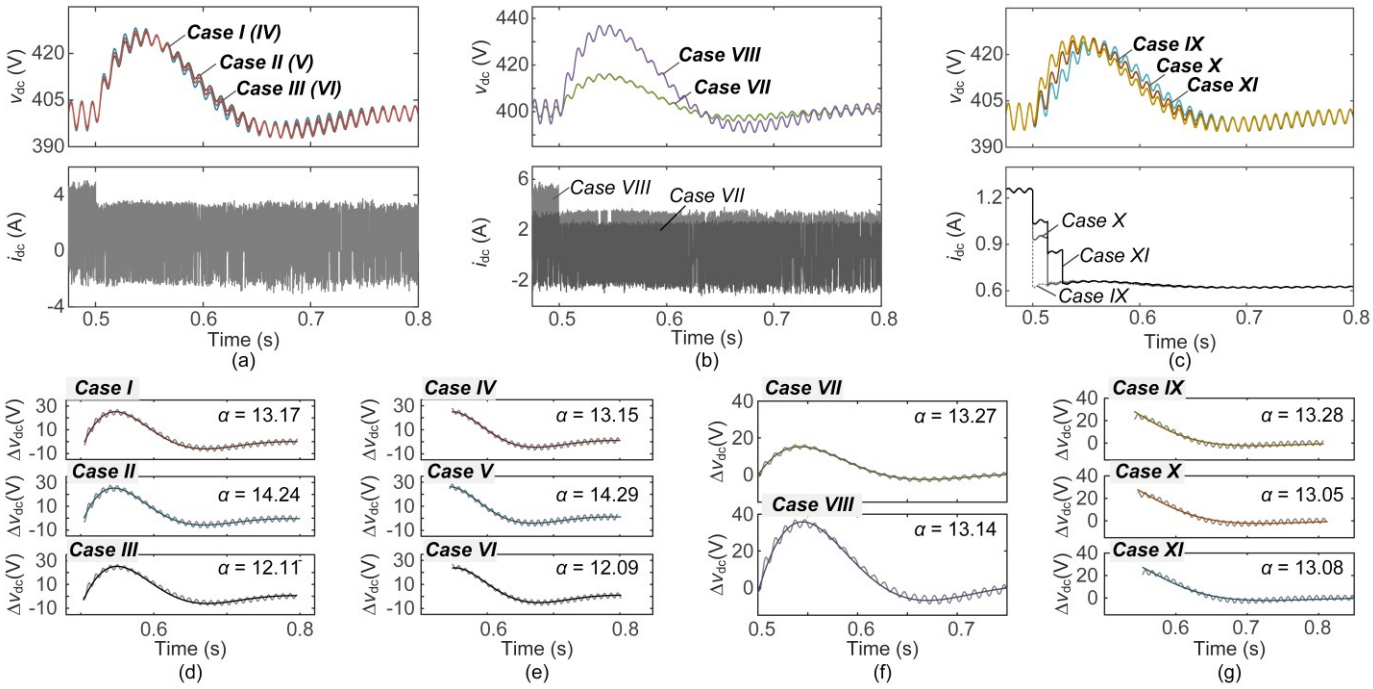

Fig. 7. Simulation results of Cases I–XI for a boost PFC [c.f. Fig. 6(a)]. (a) Simulation waveforms of Cases I–VI. (b) Simulation waveforms of Cases VII and VIII. (c) Simulation waveforms of Cases IX–XI. (d) Fitted results of Cases I–III. (e) Fitted results of Cases IV–VI. (f) Fitted results of Cases VII–VIII. (g) Fitted results of Cases IX–XI.

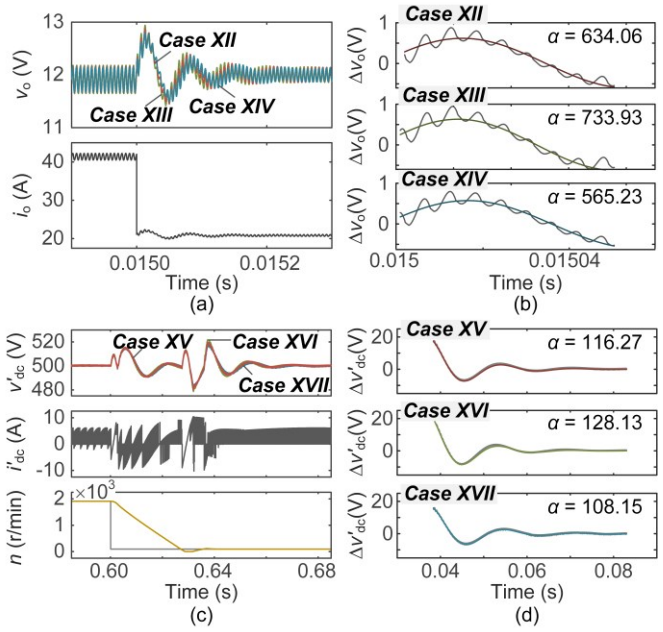

Fig. 8. Simulation results of Cases XII–XVII for an LLC converter [c.f. Fig. 6(a)] and interleaved boost converters with ASD loads [c.f. Fig. 6(b)]. (a) Simulation waveforms of Cases XII–XIV. (b) Fitted results of Cases XII–XIV. (c) Simulation waveforms of Cases XV–XVII. (d) Fitted results of Cases XV–XVII.

voltage deviation increases as the transient amplitude increases. Fig. 7(f) shows the fitted waveforms. And, the corresponding estimation results are summarized in Table IV. It is found that the proposed method is suitable for system with different transient amplitudes.

3) *Effect of Change Rate of Transient Current*

In some applications, the load current is not suddenly changed. Taking a 250-W unloading transient as an example, Fig. 7(c) shows the simulation waveforms of three different cases, i.e., Case IX (1-time current step), Case X (2-times current step), and Case XI (2-times current step). It can be seen that the maximum voltage deviation of these three cases are the same. However, the transient voltage profiles are different. As discussed in Part A of Section II, the voltage-decrease period can be used for parameter estimation. Fig. 7(g) shows the fitted waveforms. And the estimation results in Table IV illustrate the feasibility of the proposed scheme.

B. Case Study of LLC Converters and Interleaved Boost Converter-Fed ASD systems

To verify the usability of the proposed scheme for different topologies, an LLC converter (i.e., Cases XII–XIV) is chosen as a case study. Taking a 250-W load transient as an example, Fig. 8(a) shows the voltage and current waveforms of the LLC converter. Utilizing the PSO algorithm, fitted waveforms of transient voltage Δv_o are shown in Fig. 8(b). It can be seen that the fitted waveforms are consistent with the simulation waveforms. Similar to that of Case I, a pre-test of Case XII is taken to obtain R_{eq} of the LLC converter. In the pre-test, the initial capacitance $C_{o,ini}$ is 220 μF, and the fitted result of α_{ini} is 3.56. Then, R_{eq} of the LLC converter is calculated as 638.41. Based on this, estimated capacitances of Cases XII–IV are summarized in Table IV. It is found that the estimation errors are less than 1%, which demonstrates the proposed method is suitable for an isolated dc/dc converter.

Furthermore, an interleaved boost converter-fed ASD system (i.e., Cases XV–XVIII) is chosen as another case study. The detailed circuit and control parameters are also given in Fig. 6. Fig. 8(c) shows the simulation waveforms of the ASD system

TABLE IV
SIMULATION RESULTS OF 17 CASES (C.F. TABLE III)

Cases	Fitted results	Pre-test R_{eq}	C_{es} (μF)	Error
I	α=13.17, B_2=3.80×10^4, ω_d=25.07	80.92 (based on pre-test of Case I)	469.17	0.2%
II	α=14.24, B_2=6.79×10^4, ω_d=25.12		433.91	0.9%
III	α=12.11, B_2=2.11×10^4, ω_d=25.05		510.23	<0.1%
IV	α=13.15, B_2=3.75×10^4, ω_d=24.94		469.88	<0.1%
V	α=14.29, B_2=7.03×10^4, ω_d=25.08		432.40	0.6%
VI	α=12.09, B_2=2.09×10^4, ω_d=24.82		511.08	<0.1%
VII	α=13.27, B_2=2.28×10^4, ω_d=25.15		465.72	<0.1%
VIII	α=13.14, B_2=5.20×10^4, ω_d=25.06		470.24	<0.1%
IX	α=13.28, B_2=3.73×10^4, ω_d=14.50		465.30	0.2%
X	α=13.05, B_2=3.51×10^4, ω_d=14.31		473.48	0.7%
XI	α=13.08, B_2=3.82×10^4, ω_d=14.10		472.29	0.5%
XII	α=634.06, B_2=8.34×10^3, ω_d=8.00×10^4	3.56 (based on pre-test of Case XII)	221.23	0.6%
XIII	α=733.93, B_2=3.86×10^4, ω_d=8.51×10^4		191.37	0.7%
XIV	α=565.23, B_2=2.82×10^4, ω_d=7.83×10^5		248.48	0.6%
XV	α=116.27, B_2=1.51×10^3, ω_d=373.13	9.15 (based on pre-test of Case XV)	469.98	<0.1%
XVI	α=128.13, B_2=2.83×10^3, ω_d=377.09		426.48	0.8%
XVII	α=108.15, B_2=984.82, ω_d=369.69		505.27	0.9%

when a deceleration occurs. It can be seen that the dc-link voltage v'_{dc} frequently fluctuant during the deceleration processing. Referring to Fig. 8(c), the voltage profiles during low-speed phases are chosen to estimate capacitor parameters. Using the PSO algorithm, Fig. 8(d) shows the fitted waveforms of transient voltage $\Delta v'_{dc}$. Similar to that of Case I and Case XII, a pre-test of Case XV is taken to obtain R_{eq} of the front-end system. In the pre-test, the initial capacitance $C'_{dc,ini}$ is 470 μF, and the fitted result of α_{ini} is 116.27. Then, R_{eq} of the front system is calculated as 9.15. Referring to the estimated capacitances in Table IV, it can be seen that the estimation errors of Cases XV–XVII are less than 1%, which demonstrates the proposed scheme is suitable for a parallel converter system.

In summary, the simulation results verify the feasibility of the proposed TECM method. It is suitable for ac/dc and dc/dc converters with different topology structures, parameters, and transient amplitudes. However, a pre-test is required if the capacitance needs to be estimated.

IV. EXPERIMENTAL VERIFICATION

Referring to Fig. 9(a), a commercial power supply is chosen as a case study. Its rated power P is 1 kW. The input and output voltages are 110–240 VAC and 48 VDC, respectively. Notice that the power supply's housing and capacitors are disassembled to carry out the experimental study, which is not required in actual applications. Generally, the detailed circuit topology, circuit parameters, and control parameters of a commercial power supply cannot be directly obtained. However, the circuit structure is easily found (i.e., a two-stage ac/dc/dc system), as shown in the top of Fig. 9(a). Here, v_{dc}, i_{dc}, v_o, i_o denote the dc-link voltage, dc-link current, rear-end output voltage, and rear-end output current, respectively. C_{dc} and C_o represent the dc-link capacitor and output capacitor, respectively.

In order to verify the proposed CM scheme, three types of capacitors are chosen, i.e., Cap. A, Cap. B, and Cap. C. The detailed parameters of these capacitors are measured using an LCR meter operates at 120 Hz and 25 °C, as shown in Figs. 9(b)–9(d). Moreover, the switching frequency $f_{sw,ac}$ and $f_{sw,dc}$ of the front-end ac/dc converter and rear-end dc/dc converter are measured by an oscilloscope, which are about 100 kHz and 125 kHz, respectively.

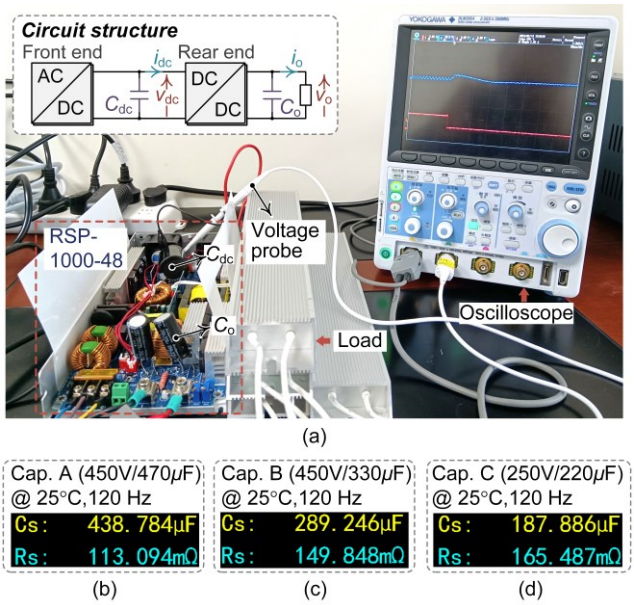

Fig. 9. Experimental setup and measured capacitor parameters. (a) Experimental setup. (b) Measured parameters of Cap. A. (c) Measured parameters of Cap. B. (d) Measured parameters of Cap. C.

Furthermore, 9 cases are chosen to comprehensively evaluate the proposed scheme. Different experimental conditions are considered, including sampling frequencies (Cases I and II), transient regions (Case III), transient amplitudes (Case IV), capacitor parameters (Cases V and VI), and topology structures (Cases VII–IX). Table V shows the detailed experimental conditions, where ΔP_o represents the change amplitude of output power, $f_{sa,ac}$ and $f_{sa,dc}$ denote the sampling frequencies of transient voltage profiles of the front-end and rear-end converters, respectively.

It should be noted that the transient voltage profiles are sampled using an oscilloscope and its voltage probe in the experiments. They can also be sampled using an MCU, which is detailed discussed in Section V. Based on the sampled data, the capacitor parameters are obtained using the PSO algorithm, which is operated in the MATLAB software.

A. Case Study of Front-end AC/DC Converter

1) *Effect of Sampling Frequency and Transient Regions*

Taking a 15%P unloading transient as an example, the top of Fig. 10(a) shows the experimental waveforms of dc-link voltage v_{dc} and load current i_o. Here, the sampling rate of the oscilloscope is defined as 25 kS/s, and the sampling frequency $f_{sa,ac}$ of the transient voltage profile is 25 kHz. Utilizing the PSO algorithm, the fitted waveforms and results are shown in the bottom of Fig. 10(a). It can be seen that the fitted curve is consistent with the transient voltage Δv_{dc}, which demonstrates the feasibility of the estimation model. In order to estimate capacitance to evaluate the accuracy, a pre-test is taken to obtain R_{eq} of the front-end ac/dc converter. In the pre-test, Cap. A is utilized, and the fitted result of α_{ini} is 13.5719. Then, R_{eq} is calculated as 83.9617. Based on the fitted result α and R_{eq}, the capacitance can be calculated, as shown in Table VI.

TABLE V
DIFFERENT EXPERIMENTAL CONDITIONS FOR 12 CASES OF THE SYSTEM SHOWN IN FIG. 9

Cases	Cap.	Experimental conditions
I	C_{dc}	Cap. A (438.78μF, 113.09 mΩ), ΔP_o=15%P, $f_{sa,ac}$=25kHz
II	C_{dc}	Cap. A (438.78μF, 113.09 mΩ), ΔP_o=15%P, $f_{sa,ac}$=2.5kHz
III	C_{dc}	Cap. A (438.78μF, 113.09 mΩ), ΔP_o=15%P, $f_{sa,ac}$=2.5kHz (different transient duration)
IV	C_{dc}	Cap. A (438.78μF, 113.09 mΩ), ΔP_o=25%P, $f_{sa,ac}$=2.5kHz
V	C_{dc}	Cap. B (289.25μF, 149.85 mΩ), ΔP_o=15%P, $f_{sa,ac}$=2.5kHz
VI	C_{dc}	Cap. B (289.25μF, 149.85 mΩ), ΔP_o=25%P, $f_{sa,ac}$=2.5kHz
VII	C_o	Cap. C (187.89μF, 165.49 mΩ), ΔP_o=15%P, $f_{sa,dc}$=125kHz
VIII	C_o	Cap. C (187.89μF, 165.49 mΩ), ΔP_o=25%P, $f_{sa,dc}$=125kHz
XI	C_o	Cap. C (187.89μF, 165.49 mΩ), ΔP_o=25%P, $f_{sa,dc}$=62.5kHz

In Case I, the ratio N of sampling frequency $f_{sa,ac}$ to switching frequency $f_{sw,ac}$ is 1/4. Actually, a lower sampling frequency can be utilized. Fig. 10(b) shows the experimental waveforms and estimation results of Case II. Here, the sampling rate of the oscilloscope is defined as 2.5 kS/s. The sampling frequency $f_{sa,ac}$ and the ratio N are 2.5 kHz and 1/40, respectively. Referring to the fitted waveforms and estimation results in Fig. 10(b) and Table VI, it can be seen that the proposed scheme is suitable for the case with a low sampling rate.

In actual applications, a whole transient waveform may not be sampled due to some reasons, such as transient detection

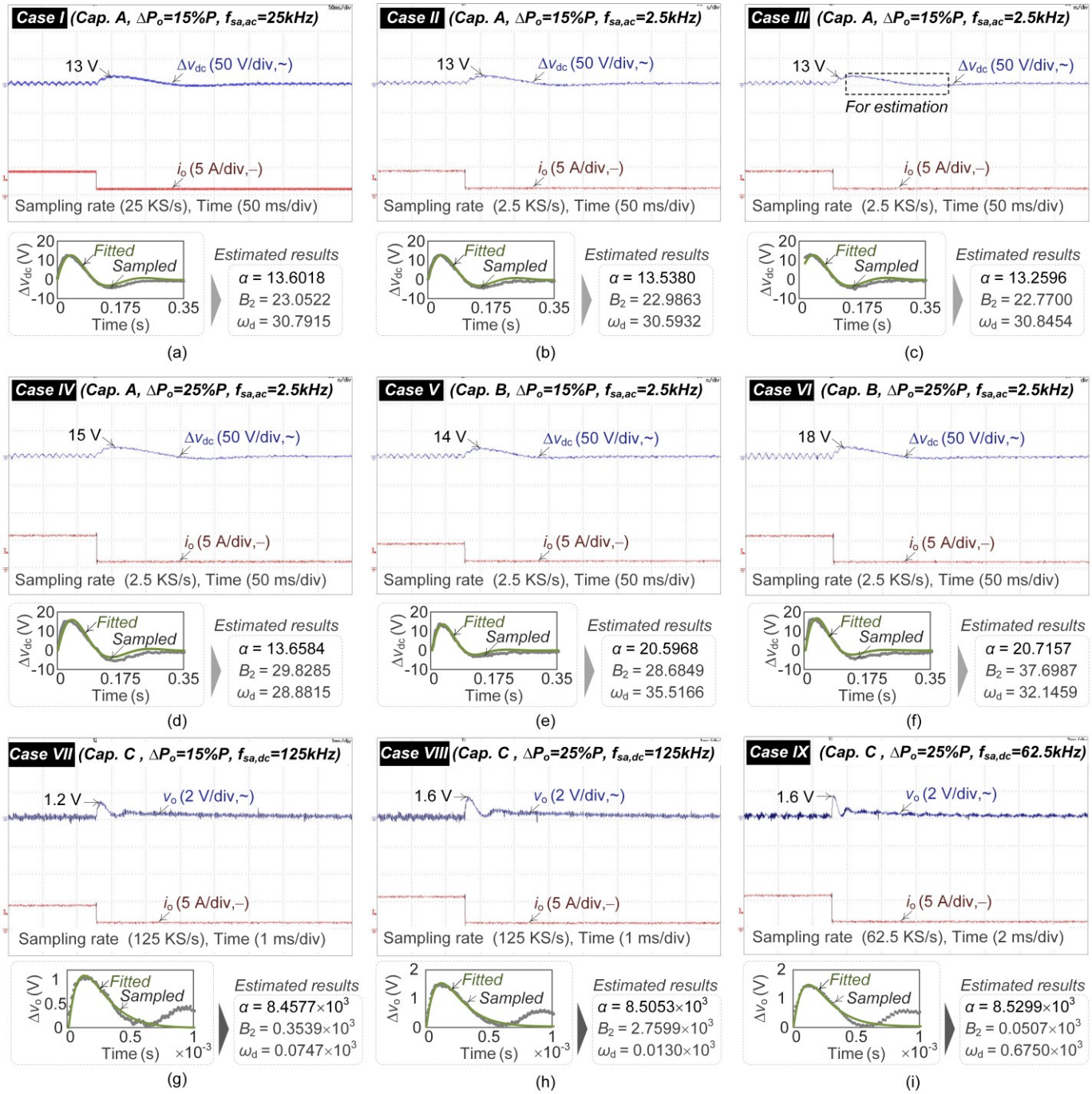

Fig. 10. Experimental waveforms and estimation results of Cases I–IX (c.f. Table V). (a) Case I. (b) Case II. (c) Case III. (d) Case IV. (e) Case V. (f) Case VI. (g) Case VII. (h) Case VIII. (i) Case IX.

TABLE VI
EXPERIMENTAL RESULTS OF CASES I–IX (C.F. TABLE V)

Cases	N (f_{sa}/f_{sw})	Estimated α	Estimated R_{eq}	Estimated capacitances	Errors
I	1/4	13.6018	83.9617 (based on pre-test of Case I)	437.82 μF	0.22%
II	1/40	13.5380		439.88 μF	0.25%
III	1/40	13.2596		438.00 μF	0.18%
IV	1/40	13.6584		436.00 μF	0.63%
V	1/40	20.5968		289.13 μF	0.04%
VI	1/40	20.7157		287.47 μF	0.62%
VII	1	8.4577×10^3	0.3148 (based on pre-test of Case VII)	187.79 μF	0.05%
VIII	1	8.5053×10^3		186.74 μF	0.61%
IX	1/2	8.5299×10^3		186.21 μF	0.89%

delay [41], [42]. In order to analyze the effect of transient regions, a region of transient voltage trajectory is used in Case III, as shown in the top of Fig. 10(c). Referring to the bottom of Fig. 10(c), it can be seen that the function of curve fitting is available. Also, the estimation results in Table VI demonstrate that the proposed scheme is feasible if a short transient region is utilized.

2) *Effect of Transient Amplitudes and Capacitor Parameters*

Considering different transient amplitudes, the top of Fig. 10(d) shows the experimental waveforms of Case IV, where the load change amplitude is 25%P. It can be seen that the maximum voltage deviation is larger than that of Fig. 10(a)–10(c) due to the relatively large change amplitude of load current. Referring to the fitted results in the bottom of Fig. 10(d), it is found that the fitted waveform is consistent with the experimental waveform. Moreover, the estimation result shown in Table VI demonstrates that the proposed scheme is suitable for converters with different transient amplitudes.

Furthermore, Figs. 10(e) and 10(f) give the experimental waveforms and estimation results of Case V and Case VI, where Cap. B is utilized. It can be seen that the estimation errors are less than 1%, which demonstrates that the proposed scheme is suitable for converters with different capacitor parameters.

B. Case Study of Rear-end DC/DC Converter

Taking the rear-end dc/dc as a case study, the top of Fig. 10(g) shows the experimental waveforms of output voltage v_o and load current i_o. Here, the sampling rate of the oscilloscope is defined as 125 kS/s, and the sampling frequency $f_{sa,\,dc}$ of the transient voltage profile is 125 kHz. Utilizing the PSO algorithm, the fitted results are shown at the bottom of Fig. 10(g). It is found that the fitted curve is consistent with that of the experimental waveform. Similar to that of the front-end ac/dc converter, a pre-test is taken to obtain R_{eq} of the dc/dc converter, in order to obtain capacitance to evaluate the estimation accuracy. In the pre-test, Cap. C is utilized, and the fitted result of α_{ini} is 8.4534×10^3. Then, R_{eq} is calculated as 0.3148. Based on the fitted result α and R_{eq}, the capacitance can be calculated, as shown in Table VI. Furthermore, Fig. 10(h) shows the experimental waveforms and fitted results of converters with different transient amplitudes (i.e., Case VIII). The corresponding estimation results shown in Table VI demonstrate that the proposed scheme is suitable for a dc/dc converter.

In Cases VII and VIII, the ratio N of sampling frequency $f_{sa,dc}$ to switching frequency $f_{sw,dc}$ is 1. A lower sampling rate is also feasible (i.e., 1/2), as shown in Fig. 10(i). Referring to the estimation results and fitted waveforms in Table VI and the bottom of Fig. 10(i), it is found that the estimation error is less than 1%, which demonstrates that the proposed scheme is suitable for different sampling frequencies.

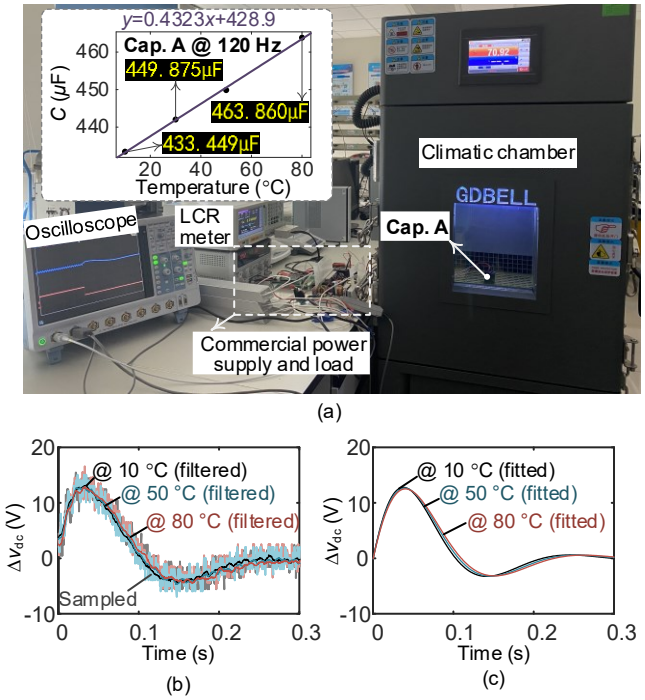

Fig. 11. Temperature testing setup and experimental results. (a) Temperature testing setup. (b) Sampled waveforms under different temperatures. (c) Fitted waveforms under different temperatures.

C. Sensitivity Analysis

Besides the above-mentioned 9 cases, the sensitivity analysis of the proposed method is given in this sub-section.

1) *Effect of Temperature Variation*

In order to verify the effect of temperature variation, Cap. A is placed in a climatic chamber and three typical temperatures (i.e., 10 °C, 50°C, and 80°C) are chosen as case studies. Fig. 11(a) shows the photograph of the built temperature testing setup. The measurement results of capacitance (using the LCR meter) at different temperatures are given in the top of Fig.11(a). It is found that the capacitance increases as the temperature increases, which is similar to that in Fig. 5(b). Furthermore, taking Case II as an example, Fig. 11(b) shows the sampled transient waveforms at different temperatures. It can be seen that there exist slight differences in the transient waveforms due to the capacitance being different at different temperatures. Utilizing the PSO algorithm, the fitted waveforms are shown in Fig. 11(c). And, the corresponding estimation results are listed in Table VII. It is found that the estimation errors are less than 1%, which demonstrates that the proposed scheme is suitable for different temperature conditions.

2) *Effect of High-Frequency Ripples and Harmonics*

In the proposed method, a moving average filtering (MAF) algorithm is used to filter the noise on sampling data [42], i.e.,

TABLE VII
EXPERIMENTAL RESULTS FOR CASE II AT DIFFERENT TEMPERATURES

Tem. (℃)	Tested C (μF)	Fitted results	Pre-test R_{eq}	C_{es} (μF)	Error
10	433.45	α=13.74, B_2=23.87, ω_d =30.29	83.9617	433.35	<0.1%
50	449.88	α=13.31, B_2=23.70, ω_d=29.25	(c.f.,	447.38	0.6%
80	463.86	α=13.94, B_2=23.44, ω_d=28.36	Case I)	460.16	0.8%

$$y_n = \left(x_n + \sum_{i=1}^{(m-1)/2} x_{n-i} + \sum_{i=1}^{(m-1)/2} x_{n+i} \right) \Big/ m \tag{9}$$

where y_n and x_n represent the filtered data and sampling data, respectively. m is the size of a sliding window. In the foregoing examples, m is defined as 20 to filter the noise signals. By adjusting m, the effect of high-frequency ripples and harmonics can be observed.

Taking Case I as an example, Fig. 12(a) shows the filtered and fitted waveforms. As m=1, the filtered waveform represents the original sampled waveform without using the filter function. Here, the signal includes the ripple and harmonic information. Furthermore, Fig. 12(b) and Fig. 12(c) show the filtered and fitted waveforms when m=175 and 250, respectively. Notice that the double-line-frequency harmonic component is the major harmonic component in v_{dc} of the boost PFC converter [50], and its frequency is 100 Hz in this case study. The double-line-frequency harmonic has been completely filtered out when m=250 due to the sampling frequency is 25 kHz. Therefore, there is almost no harmonic or ripple information in v_{dc} when m=250. The estimation results in Table VIII demonstrate that the estimation accuracy increases as m increases, which illustrates that the harmonic and ripple have a negative effect. Another test in Figs. 12(d)–12(f) also demonstrates the conclusion.

3) *Effect of Parameters Identification Algorithms*

Generally, the transient profile is mainly dependent on the load change amplitudes, circuit, and control parameters of converters. This information is usually unknown in the monitoring procedure. It is difficult to define an accurate search range of α, B_2, and ω_d in the PSO algorithm. In the proposed scheme, the low bounds for α, B_2, and ω_d are defined as 0, and there are no upper bounds. Moreover, the iterations end when the relative change in the best objective function value over the last iterations is less than 10^{-6}. Notice that although a relatively large boundary is utilized, the parameters can be accurately estimated if a transient profile is well-fitted, as shown in the foregoing experimental cases.

Moreover, only one instance of parameter estimation results of each case is given in the foregoing experimental examples. As discussed in [12], condition monitoring can be performed once a day or even once a week, dependent on the operation requirement. It is better to utilize the average value of multiple estimations to improve the accuracy. Taking Case II and Case V as examples, Fig. 13(a) shows the fitted results of 8 tests. It is found that the PSO algorithm (with a relatively large boundary) can well fit the experimental data. Furthermore, Figs. 13(b) and 13(c) show the boxplot graphs of the estimated results. It can be seen that the average errors of Case II and Case V are 0.04% and 0.19%, respectively. These 8 cases also verify the PSO algorithm can accurately identify the parameters when a relatively large boundary is set.

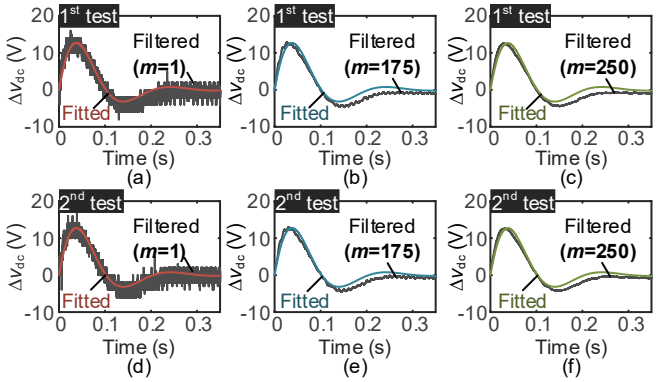

Fig. 12. Fitted results for Case I with different filter parameters. (a) The 1st test, m=1. (b) The 1st test, m=175. (c) The 1st test, m=250. (d) The 2nd test, m=1. (e) The 2nd test, m=175. (f) The 2nd test, m=250.

TABLE VIII
EXPERIMENTAL RESULTS FOR CASE I WITH DIFFERENT FILTER PARAMETERS

Cases	m	Fitted results	Pre-test R_{eq}	C_{es} (μF)	Error
1st test	1	α=13.67, B_2=23.19, ω_d =30.83	83.9617	435.85	0.67%
	175	α=13.62, B_2=23.08, ω_d=30.80	(c.f.,	437.27	0.35%
	250	α=13.58, B_2=22.99, ω_d=30.78	Table VI)	438.50	0.06%
2nd test	1	α=13.66, B_2=23.28, ω_d =30.74	83.9617	435.87	0.66%
	175	α=13.64, B_2=23.22, ω_d=30.72	(c.f.,	436.59	0.50%
	250	α=13.61, B_2=23.14, ω_d=30.70	Table VI)	437.47	0.30%

On the other hand, the PSO algorithm is utilized in the above-mentioned experimental cases. Other parameter identification algorithms also can be utilized, such as the genetic algorithm (GA) and least-squares (LS) algorithm. Taking Case II as an example, Fig. 14 shows the fitted waveforms of different algorithms, where the solutions are obtained using the "particleswarm", "ga", and "lsqcurvefit" functions in MATLAB R2021A. For the GA and LS algorithms, the boundary range of α, B_2, and ω_d are the same as that of the PSO algorithm. It is found that the GA and LS algorithms also can be used for parameter identification. The estimation accuracy is similar. However, the execution time of different algorithms is different, as summarized in Table IX. Although the LS algorithm has a relatively short execution time, initial values of α, B_2, and ω_d are required to solve the nonlinear least-squares problem. Fortunately, the parameters can be successfully identified, even if the initial values are away from the target values (i.e., the actual values). Here, the initial values of α, B_2, and ω_d are all defined as 1. Generally, the LS algorithm can be implemented in an MCU due to its simplicity [18], [51]. It is possible to utilize an MCU to operate the LS algorithm to realize the CM of capacitors.

V. APPLICATION CASES FOR WHITE-BOX AND GREY-BOX SYSTEMS

In this section, two typical application cases for a white-box system and a grey-box system are given to further illustrate the implementation of the proposed method.

A. Application of the Proposed Method in a White-Box System

In a white-box system, the existing voltage sensor for the control purpose can be reused for CM, as shown in Fig. 4.

Taking a self-designed digital-controlled boost PFC converter as an example, Fig. 15(a) shows the built experimental setup, where the circuit and control parameters

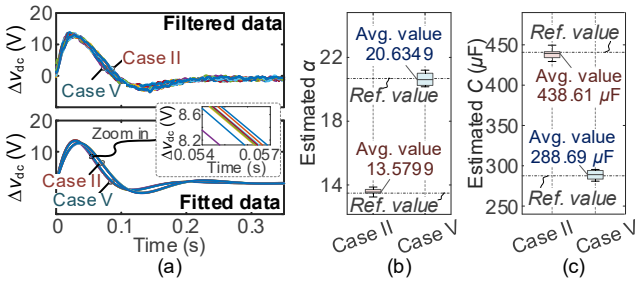

Fig. 13. Estimation results of multiple tests for Case II and Case V. (a) Fitted data. (b) Estimated results of α. (c) Estimated results of capacitance.

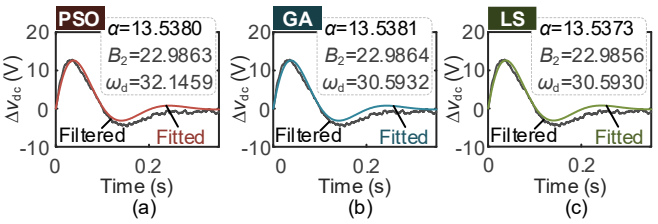

Fig. 14. Estimation results of Case II by utilizing different parameter identification algorithms. (a) PSO. (b) GA. (c) LS.

TABLE IX
ESTIMATION RESULTS FOR CASE II WITH DIFFERENT ALGORITHMS

Algo.	Error	Iteration/ generation	Elapsed time	Advantages and limitations
PSO	0.25%	60 times	0.3912 s	Not need initial values, relatively long operation time
GA	0.25%	101 times	0.6203 s	
LS	0.25%	5 times	0.0130 s	Need initial values, relatively short operation time

can be found in [42]. Here, the existing voltage sensor and MCU are used for control and CM purposes. The rate power P_r of the converter is 1 kW. In the proposed scheme, the unloading transient is detected based on a comparison between the dc-link voltage v_{dc} and designed threshold voltage V_{th}, as shown in Fig. 15(b). In order to prevent false detection, two times comparisons are introduced in the detection process. Moreover, V_{th} should be larger than the sum of reference voltage V_{ref} and maximum ripple voltage $\Delta V_{dc,max}$, i.e., $V_{th} > V_{ref} + \Delta V_{dc,max}$. Considering the transient occurrence period (e.g., 10 min [41]) is considerably short compared with capacitor aging [in the order of hour, c.f., Fig. 5(a)], V_{th} can be set relatively large. Then, a transient with a relatively large amplitude is selected for CM.

On the other hand, the time t is a key variable in the transient behavior model, i.e., Eq. (2). It is necessary to record the data and its corresponding sampling instant if an MCU is utilized for sampling. Fig. 15(c) shows the timeline acquisition flowchart, where T_{sa} is the sampling period. $v_{dc,st}$ and n_{st} represent the sampled steady-state data and the serial number of sampling points. $v_{dc,tr}$ and n_{tr} represent the sampled transient data and corresponding serial number. n'_{st} is the serial number at the initial instant of transients. By merging the steady-state and transient data, the timeline of transient profile can be obtained, i.e., $t=(n_{st}+n_{tr}-n'_{st})T_{sa}$.

Taking a 32%P_{tr} unloading transient as an example, Fig. 15(d) shows the experimental waveforms. Here, Cap. A is utilized. This case is a pre-test to obtain R_{eq} of this PFC converter. Following the flowchart in Fig. 4(b), R_{eq} is calcula-

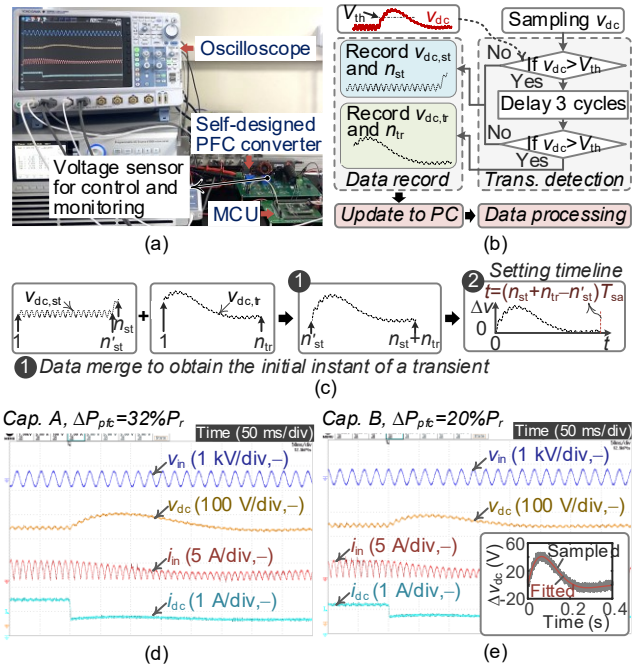

Fig. 15. Application case of a white-box system. (a) Experimental setup. (b) Transient detection flowchart. (c) Timeline acquisition flowchart. (d) Experimental waveforms for a 32%P_r unloading transient. (e) Experimental waveforms and estimation results for a 20%P_r unloading transient.

ted as 166.8402. Furthermore, Cap. B and a 20%P_{tr} transient condition are considered to verify the proposed method, as shown in Fig. 15(e). In this case, V_{th} is set as 420 V, and the sampling frequency is 5 kHz. n_{st} and n_{tr} are set as 512 and 2048, respectively. Referring to the bottom of Fig. 15(e), it can be seen that the fitted curve is consistent with the sampled data. Also, the fitted results of α, B_2, and ω_d are 10.4856, 99.6669, and 14.4375, respectively. The estimated capacitance and estimation error are 285.81 μF and 1.1%, respectively.

B. Application of the Proposed Method in a Grey-Box System

As discussed in Section II, an additional voltage sensor may require for a grey-box system (e.g., a commercial converter) if the signal interface has not been provided by manufacturers.

Taking the previously used commercial power supply as a case study, Fig. 16(a) shows the built setup. Two self-powered sampling circuits are designed to obtain v_{dc} and v_o, respectively. The typical structure is shown in the bottom of Fig. 16(a). Here, two MOSNSUN power modules PV20-27A15 (for 200–1100 Vdc) and URA4815YMD (for 18–75 Vdc) are utilized for self-power. And the voltage sensor LV 25-P is used for voltage sampling. Taking Circuit II as an example, Fig. 16(b) shows the PCB prototype of the designed sampling circuit.

Taking a 25%P unloading transient as an example, Fig. 16(c) shows the experimental waveforms of the front-end ac/dc converter (Cap. A is utilized), where $v_{dc,sa}$ represents the output signal of the designed sampling circuit. It is sampled by an MCU TMS320F28377D and being transferred to the PC using a data transmission module. Utilizing the PSO algorithm, the bottom of Fig. 16(c) shows the fitted results. Here, V_{th} is set as 420 V, and the sampling frequency is 5 kHz. n_{st} and n_{tr} are set as 256 and 1280, respectively. The fitted values of α, B_2, and ω_d

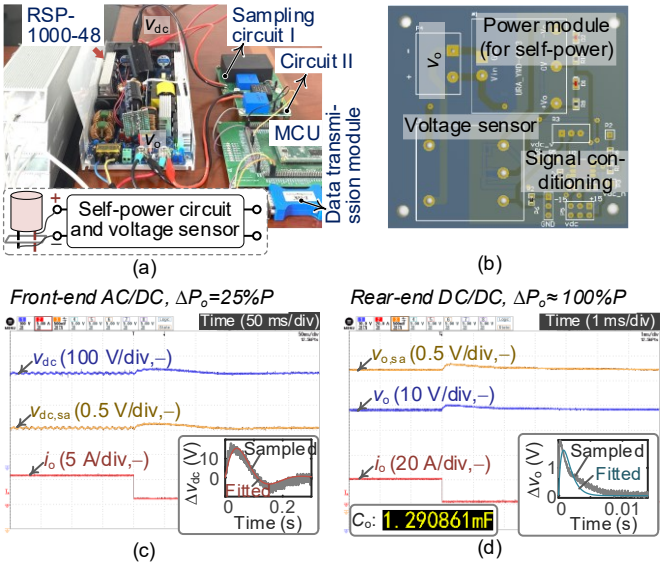

Fig. 16. Application case of a grey-box system. (a) Experimental setup. (b) PCB prototype of the sampling circuit II. (c) Experimental results for a 25%P unloading transient. (d) Experimental results for a 100%P unloading transient.

are 13.6239, 29.4641, and 28.4213, respectively. As R_{eq} = 83.9617 (based on pre-test of Case I), the estimated capacitance and estimation error are 437.11 μF and 0.4%, respectively.

Taking about 100%P unloading transients as an example, Fig. 16(d) shows the experimental waveform of rear-end converter, where $v_{o,sa}$ represents the output signal of the designed sampling circuit. Here, the change amplitude of the output current is about 20 A, which reaches the maximum value of the commercial converter. Also, the used capacitance is 1290.86 μF (@25°C, 120 Hz). Utilizing the PSO algorithm, the bottom of Fig. 16(d) shows the fitted results. Here, V_{th} is set as 49 V, and the sampling frequency is 25 kHz. n_{st} and n_{tr} are set as 256 and 512, respectively. The fitted values of α, B_2, and ω_d are 1253.99, 149.77, and 37.12, respectively. As R_{eq} = 0.3148 (based on pre-test of Case VII), the estimated capacitance and estimation error are 1266.59 μF and 1.8%, respectively. The experimental results demonstrate that the CM function is normally operated when a relatively large load transient occurs. However, the transient waveform is a little distorted compared with the waveforms in Figs. 10(g)–10(i) due to such a large load step occurs. The estimation error is relatively large. Fortunately, the average value of multiple estimations (i.e., multiple transients in different amplitudes) can be used to improve the estimation accuracy.

VI. Conclusion

This paper proposes a transient equivalent circuit model-based grey-box method for online monitoring of dc-link capacitors. The main contributions and remarks are given in the following.

A. Main Contributions

1) By analyzing the transient behavior of ac/dc and dc/dc converters, it is found that the transient trajectory is similar to a zero-state response of a parallel RLC circuit. Based on this, dc-link capacitors can be online monitored using the transient trajectory with minimum dependency on the detailed topology and control information. Besides, it has features of relatively high applicability and extreme low sampling frequency.

2) The feasibility of the proposed scheme has been verified on an ac/dc and a dc/dc system with converter and inverter loads in simulation. Moreover, its feasibility has been demonstrated in a commercial power supply. Experimental results illustrate that the estimation errors of the damping factor α and dc-link capacitance are less than 1%. Furthermore, two typical application cases for a white-box system and a grey-box system are given to further illustrate the implementation of the proposed method.

B. Brief Remarks

Comparing with the existing schemes, brief remarks are given in the following.

1) As discussed in [40]–[42], the transient trajectory has the features of large amplitude and long duration, which is easily to be sampled. Although additional ripple extraction circuits and high-speed sampling devices are not required in [40]–[42], additional current sensors [40] and unique estimation models [40]–[42] limit their extensibility. Different from that, the proposed method is independent of circuit topology. It can be used for CM of ac/dc and dc/dc converters and it has a strong adaptability.

2) The proposed scheme is feasible even if an extreme low sampling frequency is utilized (e.g., 1/40 of the switching frequency), which can reduce the hardware cost of sampling systems and the volume of sampled data.

3) The proposed method can be used for a grey-box system with minimum dependency on the detailed topology and control information However, an additional voltage sensor is needed to sample the transient voltage. Fortunately, additional sensors are not required if the function is integrated in the design phase.

4) One limitation of the proposed scheme is that a pre-test is required if the user wants to obtain detailed capacitance parameters. Fortunately, the damping factor α (related to capacitance) of transient trajectories of converters can be chosen as a new health indicator of capacitors.

5) Besides the PSO algorithm, other algorithms (e.g., GA and LS) also can be utilized for parameter identification. Comparing with the PSO and GA algorithms, the LS algorithm is simpler and it can be implemented in an MCU [18], [51]. However, the detailed design of the CM using an MCU needs further investigation in the future.

References

[1] H. Wang and F. Blaabjerg, "Reliability of capacitors for dc-link applications in power electronic converters-an overview," *IEEE Trans. Ind. Appl.*, vol. 50, no. 5, pp. 3569–3578, Sep. 2014.

[2] A. Kyriakidou, N. Karelos, and A.Delis, "Video-streaming for fast moving users in 3G mobile networks," in *Proc. 4th ACM Int. Workshop Data Eng. Wireless Mobile Access*, 2005, pp. 65–72.

[3] Z. Zhao, P. Davari, W. Lu, H. Wang and F. Blaabjerg, "An overview of condition monitoring techniques for capacitors in dc-link applications," *IEEE Trans. Power Electron.*, vol. 36, no. 4, pp. 3692-3716, Apr. 2021.

[4] Z. Zhao, D. Zhou, P. Davari, J. Fang, and F. Blaabjerg, "Reliability analysis of capacitors in voltage regulator modules with consecutive load

transients," *IEEE Trans. Power Electron.,* vol. 36, no. 3, pp. 2481-2487, March 2021.

[5] Z. Zhao, D. Zhou, H. Wang, P. Davari, and F. Blaabjerg, "Reliability improvement of voltage regulator modules by a virtual series voltage source," *IEEE Trans. Ind. Electron.*, vol. 69, no. 12, pp. 12641-12652, Dec. 2022.

[6] H. Wang and F. Blaabjerg, "Power electronics reliability: State of the art and outlook," *IEEE J. Emerg. Sel. Topics Power Electron.*, vol. 9, no. 6, pp. 6476–6493, Dec. 2021.

[7] Z. Zhao, H. Hu, Z. He, H. H. -C. Iu, P. Davari and F. Blaabjerg, "Power electronics-based safety enhancement technologies for lithium-ion batteries: an overview from battery management perspective," *IEEE Trans. Power Electron.,* vol. 38, no. 7, pp. 8922-8955, July 2023.

[8] E. Farjah, H. Givi, and T. Ghanbari, "Application of an efficient Rogowski coil sensor for switch fault diagnosis and capacitor ESR monitoring in nonisolated single switch DC-DC converters," *IEEE Trans. Power Electron.*, vol. 32, no. 2, pp. 1442–1456, Feb. 2017.

[9] L. Ren, C. Gong and Y. Zhao, "An online ESR estimation method for output capacitor of boost converter," *IEEE Trans. Power Electron*., vol. 34, no. 10, pp. 10153-10165, Oct. 2019.

[10] W. Lu, X. Lu, J. Han, Z. Zhao and X. Du, "Online estimation of ESR for dc-link capacitor of boost PFC converter using wavelet transform based time-frequency analysis method," *IEEE Trans. Power Electron*., vol. 35, no. 8, pp. 7755-7764, Aug. 2020.

[11] M. W. Ahmad, N. Agarwal, and S. Anand, "Online monitoring technique for aluminum electrolytic capacitor in solar PV-based DC system," *IEEE Trans. Ind. Electron.*, vol. 63, no. 11, pp. 7059–7066, Nov. 2016.

[12] K. Yao, H. Li, L. Li, C. Guan; L. Li, Z. Zhang, and J. Chen, "A noninvasive online monitoring method of output capacitor's *C* and ESR for DCM flyback converter," *IEEE Trans. Power Electron*., vol. 34, no. 6, pp. 5748–5763, Jun. 2019.

[13] K. Yao, W. Tang, X. Bi, and J. Lyu, "An online monitoring scheme of DC-link capacitor's ESR and C for a boost PFC converter," *IEEE Trans. Power Electron.*, vol. 31, no.8, pp. 5944-5951, Aug. 2016.

[14] C. Wu, J. Yue, J. Liu, and L. Wang, "An online proactive health monitoring method for output capacitors of vehicular auxiliary converter," *IEEE J. Emerg. Sel. Topics Power Electron*., vol. 10, no. 1, pp. 1219-1231, Feb. 2022.

[15] B. Wang, J. Meng, and P. Zhao, "Aging condition monitoring for aluminum electrolytic capacitor in variable speed drives," *IEEE Trans. Power Electron.*, vol. 37, no. 4, pp. 4564-4574, April 2022.

[16] M. W. Ahmad, P. N. Kumar, A. Arya and S. Anand, "Noninvasive technique for dc-link capacitance estimation in single-phase inverters," *IEEE Trans. Power Electron.*, vol. 33, no. 5, pp. 3693–3696, May 2018.

[17] N. Zhao, R. Gao, G. Wang, D. Ding, G. Zhang and D. Xu, "Online estimation method of dc-link capacitors for reduced dc-link capacitance IPMSM drives," *IEEE Trans. Power Electron.*, vol. 36, no. 11, pp. 12196-12201, Nov. 2021.

[18] N. Agarwal, M. W. Ahmad, and S. Anand, "Quasi-online technique for health monitoring of capacitor in single-phase solar inverter," *IEEE Trans. Power Electron.*, vol. 33, no. 6, pp. 5283–5291, Jun. 2018.

[19] P. Sun, C. Gong, X. Du, Q. Luo, H. Wang, and L. Zhou, "Online condition monitoring for both IGBT module and DC-link capacitor of power converter based on short-circuit current simultaneously," *IEEE Trans. Ind. Electron.*, vol. 64, no. 5, pp. 3662–3671, May 2017.

[20] T. H. Nguyen and D. C. Lee, "Deterioration monitoring of DC-link capacitors in AC machine drives by current injection," *IEEE Trans. Power Electron.*, vol. 30, no. 3, pp. 1126–1130, Mar. 2015.

[21] T. Meng and P. Zhang, "An online dc-link capacitance estimation method for motor drive systems based on an intermittent reverse-charging control strategy," *IEEE Trans. Power Electron.*, vol. 38, no. 2, pp. 2481-2492, Feb. 2023.

[22] Z. Cen and P. Stewart, "Condition parameter estimation for photovoltaic buck converters based on adaptive model observers," *IEEE Trans. Rel.*, vol. 66, no. 1, pp. 148–160, Mar. 2017.

[23] L. Ren and C. Gong, "Modified hybrid model of boost converters for parameter identification of passive components," *IET Power Electron.*, vol. 11, no. 4, pp. 764-771, Apr. 2018.

[24] M. W. Ahmad, N. Agarwal, P. N. Kumar, and S. Anand, "Low-frequency impedance monitoring and corresponding failure criteria for aluminum electrolytic capacitors," *IEEE Trans. Ind. Electron.*, vol. 64, no. 7, pp. 5657–5666, Jul. 2017.

[25] B. Li and K. Low, "Low sampling rate online parameters monitoring of DC-DC converters for predictive maintenance using biogeography-based optimization," *IEEE Trans. Power Electron*., vol. 31, no. 4, pp. 2870-2879, Apr. 2016.

[26] Y. Peng, S. Zhao and H. Wang, "A digital twin-based estimation method for health indicators of dc–dc converters," *IEEE Trans. Power Electron.*, vol. 36, no. 2, pp. 2105-2118, Feb. 2021.

[27] W. Miao, K. H. Lam and P. W. T. Pong, "Online monitoring of aluminum electrolytic capacitors in photovoltaic systems by magnetoresistive sensors," *IEEE Sensors J.,* vol. 20, no. 2, pp. 767-777, 15 Jan.15, 2020.

[28] K. Laadjal, M. Sahraoui, and A. J. M. Cardoso, "On-line fault diagnosis of dc-link electrolytic capacitors in boost converters using the STFT technique," *IEEE Trans. Power Electron.*, vol. 36, no. 6, pp. 6303–6312, Jun. 2021.

[29] C. Li, Y. Yu, Z. Yang, Q. Liu, and X. Peng, "ESR estimation for aluminum electrolytic capacitor of power electronic converter based on compressed sensing and wavelet transform," *IEEE Trans. Ind. Electron.*, vol. 69, no. 2, pp. 1948–1957, Feb. 2022.

[30] K. Hasegawa, S. Nishizawa, and I. Omura, "A condition-monitoring method of dc-link capacitors used in a high-power three-phase PWM inverter with an evaluation circuit," *IEEJ J. Ind. Appl.*, vol. 8, no. 3, pp. 480-487, May 2019.

[31] P. Sundararajan, M. Sathik, F. Sasongko, C. Tan, J. Pou, F. Blaabjerg, and A. Gupta, "Condition monitoring of dc-link capacitors using goertzel algorithm for failure precursor parameter and temperature estimation," *IEEE Trans. Power Electron.,* vol. 35, no. 6, pp. 6386-6396, June 2020.

[32] M. A. Vogelsberger, T. Wiesinger, and H. Ertl, "Life-cycle monitoring and voltage-managing unit for dc-link electrolytic capacitors in PWM converters," *IEEE Trans. Power Electron.*, vol. 26, no. 2, pp. 493–503, Feb. 2011.

[33] Y. Liu, J. Bai, M. Huang, and X. Zha, "An online monitoring method for single aluminum electrolytic capacitor in the dc bank of single-phase inverter based on the Rogowski coil," *IEEE Trans. Power Electron.*, vol. 37, no. 10, pp. 12647-12658, Oct. 2022.

[34] D. Xiang, Y. Zheng, H. Li, Y. Gu, N. Zhao and J. Zheng, "Online ESR monitoring of dc-link capacitor in voltage-source-converter using damping characteristic of switching ringings," *IEEE Trans. Power Electron.*, vol. 36, no. 7, pp. 7429-7441, July 2021.

[35] S. Zhao and H. Wang, "Enabling data-driven condition monitoring of power electronic systems with artificial intelligence: Concepts, tools, and developments," *IEEE Power Electron. Mag.*, vol. 8, no. 1, pp. 18–27, Mar. 2021.

[36] H. Soliman, P. Davari, H. Wang and F. Blaabjerg, "Capacitance estimation algorithm based on DC-link voltage harmonics using artificial neural network in three-phase motor drive systems," in *Proc. IEEE Energy Convers. Congress Expo.*, 2017, pp. 5795-5802.

[37] T. McGrew, V. Sysoeva, C.-H. Cheng, C. Miller, J. Scofield, and M. J. Scott, ''Condition monitoring of dc-link capacitors using time–frequency analysis and machine learning classification of conducted EMI,'' *IEEE Trans. Power Electron.*, vol. 37, no. 10, pp. 12606–12618, Oct. 2022.

[38] H. Dang, H. Park, S. Kwak, and S. Choi, "DC-link electrolytic capacitors monitoring techniques based on advanced learning intelligence techniques for three-phase inverters," *Machines*, vol. 10, no. 12, p. 1174, Dec. 2022.

[39] H. Park, J. Kim, and S. Kwak, "Deep learning-based estimation technique for capacitance and ESR of input capacitors in single-phase DC/AC converters," *J. Power Electron.*, vol. 22, pp. 513–521, Dec. 2022.

[40] Z. Zhao, W. Lu, P. Davari, X. Du, H. H. Iu, and F. Blaabjerg, "An online parameters monitoring method for output capacitor of buck converter based on large-signal load transient trajectory analysis," *IEEE J. Emerg. Sel. Topics Power Electron*., vol. 9, no. 4, pp. 4004-4015, Aug. 2021.

[41] Z. Zhao, P. Davari, Y. Wang and F. Blaabjerg, "Online capacitance monitoring for dc/dc boost converters based on low-sampling-rate approach," *IEEE J. Emerg. Sel. Topics Power Electron*., vol. 10, no. 5, pp. 5192-5204, Oct. 2022.

[42] Z. Zhao, P. Davari, W. Lu, and F. Blaabjerg, "Online dc-link capacitance monitoring for digital-controlled boost PFC converters without additional sampling devices," *IEEE Trans. Ind. Electron.*, vol. 70, no. 1, pp. 907-920, Jan. 2023.

[43] Z. Zhao, A. Geng, H. Tao, H. Hu, and Z. He, "A method, apparatus, equipment and storage medium for online monitoring of dc-link capacitance," China Patent CN114740272B, Mar. 2023.

[44] J. W. Nilsson and S. Riedel, *Electric Circuits*, 9th ed. Englewood Cliffs, NJ, USA: Prentice-Hall, 2011.

[45] S. Dusmez and B.Akin, "An accelerated thermal aging platform to monitor fault precursor on-state resistance," in *Proc. IEEE Int. Electric. Mach. Drives Conf.*, 2015, pp. 1352–1358.

[46] E. Ugur, F. Yang, S. Pu, S. Zhao, and B. Akin, "Degradation assessment

and precursor identification for SiC MOSFETs under high temp cycling," *IEEE Trans. Ind. Appl.*, vol. 55, no. 3, pp. 2858–2867, May 2019.
[47] Wurth Electronics Group, Germany, "Aluminum electrolytic/Aluminum polymer capacitors," 2023. [Online]. Available: https://redexpert.we-online.com/redexpert/#/module/20/productdata/=860040875005/code/asc/contains:860040875005
[48] muRata, Nagaokakyo, Japan, "Multilayer ceramic capacitor," 2023. [Online]. Available: https://ds.murata.co.jp/simsurfing/mlcc.html?lcid=en-us#
[49] N. Chemi-Con, "Judicious use of aluminum electrolytic capacitor," Nippon Chemi-Con, Tokyo, Japan, Tech. Note, CAT. No. E1001-L, 2011.
[50] S. Li, W. Lu, S. Yan and Z. Zhao, "Improving dynamic performance of boost pfc converter using current-harmonic feedforward compensation in synchronous reference frame," *IEEE Trans. Ind. Electron.*, vol. 67, no. 6, pp. 4857-4866, June 2020.
[51] K. Abdennadher, P. Venet, G. Rojat, J. M. Retif, and C. Rosset, "A real-time predictive-maintenance system of aluminum electrolytic capacitors used in uninterrupted power supplies," *IEEE Trans. Ind. Appl.*, vol. 46, no. 4, pp. 1644–1652, Jul./Aug., 2010.

Zhaoyang Zhao (Member, IEEE) received the B.S. and M.S. degrees in electrical engineering from Northeast Agricultural University, Harbin, China, in 2014 and 2017, respectively, and the Ph.D. degree in electrical engineering from Chongqing University, China, 2020. From 2019 to 2020, he was a Visiting Ph.D. Student with the Department of Energy Technology, Aalborg University, Aalborg, Denmark. From 2021 to 2022, he was with Zhengzhou University, as an Assistant Professor. He joined Southwest Jiaotong University, in 2022, as Assistant Professor. His research interests include condition monitoring, safety and reliability assessment of power electronic converters and battery systems.

Dr. Zhao received a Prize Paper Award of the IEEE Journal of Emerging and Selected Topics in Power Electronics in 2021. He was a recipient of the Excellent Doctoral Dissertation of Chongqing City in 2022. He has served as a Guest Editor-in-Chief for Microelectronics International and a Guest Associate Editor for CPSS Transactions on Power Electronics and Applications. He is an Associate Editor of Circuit World.

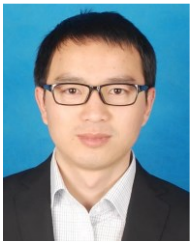

Haitao Hu (Senior Member, IEEE) received the B.S. degree from Zhengzhou University, Zhengzhou, China, in 2010, and the Ph.D. degree from Southwest Jiaotong University, Chengdu, China, in 2014, both in electrical engineering.

He is currently a Professor with the School of Electrical Engineering, Southwest Jiaotong University. His main research interests include power quality and stability of the electric traction system.

Zhengyou He (Senior Member, IEEE) received the B.Sc. degree and M. Sc. degree from Chongqing University, Chongqing, China, in 1992 and 1995, respectively, and the Ph.D. degree from Southwest Jiaotong University, Chengdu, China, in 2001.

He is currently a Professor in the School of Electrical Engineering at Southwest Jiaotong University. His research interests include signal process and information theory applied to power systems, and the application of wavelet transforms in power systems.

Weiguo Lu (Member, IEEE) received the B.S., M.S., and Ph.D. degrees in electrical engineering from Chongqing University, Chongqing, China, in 2000, 2003, and 2008, respectively.

He is currently a Professor in the School of Electrical Engineering, Chongqing University, Chongqing. He is the author or coauthor of more than 20 papers in journal or conference proceedings. His current research interests include the stability analysis and control strategies of switching power converters, and magnetic-resonance wireless power transfer.

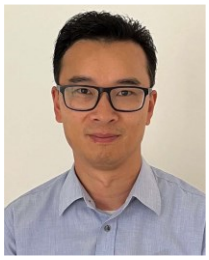

Herbert Ho Ching Iu (Senior Member, IEEE) received the B.Eng. degree (Hons.) in electrical and electronic engineering from The University of Hong Kong in 1997 and the Ph.D. degree from The Hong Kong Polytechnic University in 2000.

In 2002, he joined the School of Engineering, The University of Western Australia, as a Lecturer, where he is currently a Professor. His research interests include power electronics, renewable energy, nonlinear dynamics, current sensing techniques, and memristive systems. He has published over 100 papers in these areas. He has won two IET Premium Awards in 2012 and 2014. In 2014, he also won the Vice-Chancellor's Mid-Career Research Award. He received the 2019 IEEE Transactions on Very Large Scale Integration (VLSI) Systems Best Paper Award. He currently serves as an Associate Editor for IEEE Transactions on Circuits and Systems— II: Express Briefs, IEEE Transactions on Power Electronics, and IEEE Transactions on Network Science and Engineering; and an Editor for IEEE Transactions on Smart Grid. He is a Co-Editor of Control of Chaos in Nonlinear Circuits and Systems (Singapore: World Scientific, 2009) and Development of Memristor Based Circuits (Singapore: World Scientific, 2013).

Frede Blaabjerg (Fellow, IEEE) received the Ph.D. degree in electrical engineering from Aalborg University, Aalborg, Denmark, in 1995.

He was with ABB-Scandia, Randers, Denmark, from 1987 to 1988. He became an Assistant Professor in 1992, an Associate Professor in 1996, and a Full Professor of power electronics and drives in 1998 at Aalborg University, where he became a Villum Investigator in 2017. He is also honoris causa at Universitatea Politehnica Timisoara (UPT), Romania, and the Tallinna University of Technology (TTU), Tallinn, Estonia. He has published more than 600 journal articles in the fields of power electronics and its applications. He is a coauthor of four monographs and editor of ten books in power electronics and its applications. His current research interests include power electronics and its applications, such as in wind turbines, PV systems, reliability, harmonics, and adjustable speed drives.

Dr. Blaabjerg received 32 IEEE Prize Paper Awards, the IEEE Power Electronics Society (PELS) Distinguished Service Award in 2009, the EPE-PEMC Council Award in 2010, the IEEE William E. Newell Power Electronics Award in 2014, the Villum Kann Rasmussen Research Award in 2014, the Global Energy Prize in 2019, and the 2020 IEEE Edison Medal. He was nominated in 2014–2019 by Thomson Reuters to be between the most 250 cited researchers in engineering in the world. He was the Editor-in-Chief of IEEE Transactions on Power Electronics from 2006 to 2012. He was a Distinguished Lecturer of the IEEE Power Electronics Society from 2005 to 2007 and the IEEE Industry Applications Society from 2010 to 2011 and 2017 to 2018. From 2019 to 2020, he has served as the President of the IEEE Power Electronics Society. He is also the Vice-President of the Danish Academy of Technical Sciences.

He is nominated in 2014-2020 by Thomson Reuters to be between the most 250 cited researchers in Engineering in the world.

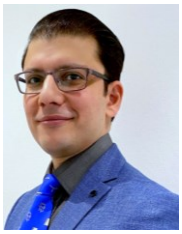

Pooya Davari (Senior Member, IEEE) received the B.Sc. and M.Sc. degrees in electronic engineering in 2004 and 2008, respectively, and the Ph.D. degree in power electronics from QUT, Australia, in 2013. From 2005 to 2010, he was involved in several electronics and power electronics projects as a Development Engineer. From 2013 to 2014, he was with QUT, as a Lecturer. He joined Aalborg University (AAU), in 2014, as a Postdoc, where he is currently an Associate Professor.

He has been focusing on EMI, power quality and harmonic mitigation analysis and control in power electronic systems. He has published more than 180 technical papers. Dr. Davari served as a Guest Associate Editor of IET journal of Power Electronics, IEEE Access Journal, Journal of Electronics and Journal of Applied Sciences. He is an Associate Editor of Journal of Power Electronics, IET Electronics, Editorial board member of Journal of Applied Sciences and Journal of Magnetics. He is member of the International Scientific Committee (ISC) of EPE (ECCE Europe) and a member of Joint Working Group six and Working Group eight at the IEC standardization TC77A. Dr.

Davari is the recipient of Equinor 2022 Prize and 2020 IEEE EMC Society Young Professional Award for his contribution to EMI and Harmonic Mitigation and Modeling in Power Electronic Applications. He is currently Editor-in-Chief of Circuit World Journal. He is founder and chair of IEEE EMC SOCIETY CHAPTER DENMARK and Leader of EMI/EMC in Power Electronics Research Group at AAU Energy.